Adaptive isolation system combining low-friction sliding pendulum bearings and SMA-based gap dampers

Dario De Domenico [1*], Emanuele Gandelli [2], Virginio Quaglini [2]

[1] Department of Engineering, University of Messina, Contrada Di Dio, 98166 Sant'Agata, Messina, Italy
[2] Department of Architecture, Built Environment and Construction Engineering, Politecnico di Milano, Piazza Leonardo da Vinci 31, 20133 Milano, Italy

* Corresponding author: Dario De Domenico, University of Messina. Email: dario.dedomenico@unime.it

ABSTRACT

The flag-shaped hysteretic behavior of Shape Memory Alloys (SMAs) can be conveniently used for developing efficient isolation systems, providing energy dissipation without implying residual displacements. This work presents a base isolation layout that combines low-friction curved surface sliders (CSSs) with SMA gap dampers (SMAGDs). The proposed SMAGDs are formed by a group of SMA wires placed in parallel with the CSS isolation system and connected to it through a sliding pin and a slotted ring in order to accomplish the "gap damper" feature. Based on this installation configuration, SMAGDs introduce additional stiffening and energy dissipation to the isolation system only when the displacement of the CSS exceeds a certain threshold or gap displacement d_{gap}, while not being engaged for lower displacements. Consequently, the system exhibits a phased behavior, meaning that its reaction force depends on the amplitude of the displacement. This is particularly convenient for limiting seismic displacements while avoiding at the same time undesirable effects such as high structural accelerations and poor re-centering capability exhibited by alternative systems at low-intensity excitations, e.g. systems based on high-friction CSSs or combinations of CSSs with traditional supplemental energy dissipation devices. The paper describes a preliminary design procedure and the evaluation of the seismic performance of the proposed CSS+SMGAGD system. A leading design parameter of the SMAGDs is the overall cross-sectional area of the SMA wires, which can be designed through a displacement spectral analysis, by introducing some reasonable assumptions for the definition of the linear equivalent mechanical properties of CSS, SMAGD and combined CSS+SMAGD system. This performance-oriented design procedure is aimed at achieving a target displacement demand of the combined CSS+SMAGD system under the maximum credible design earthquake. A parametric study comprising a variety of CSS and SMAGD properties reveals that the proposed isolation layout is suitable to limit the maximum displacement under ultimate limit state earthquakes, providing at the same time satisfactory energy dissipation along with high re-centering capability, and outperforms both low-friction CSSs and high-friction CSSs.

KEY WORDS: Base isolation; Curved surface slider; Shape memory alloys; Superelastic effects; Displacement demand; Re-centering capability; Gap damper; Friction coefficient; Sliding pendulum bearings.

1. INTRODUCTION

Seismic isolation represents an effective strategy to protect civil engineering structures and their contents from strong earthquakes. Low lateral stiffness devices are interposed between the structure and its foundations in order to decouple the movement of the superstructure from the oscillations induced by the ground shaking during an earthquake event. Seismic isolation has been recognized as a mature and reliable technology by physical observations in earthquakes, as well as by experimental shake-table tests and numerical studies [1]-[4]. Typical isolation devices include elastomeric bearings [5] and sliding supports with curved surfaces [6], the latter originally introduced in North America under the trademark name of Friction Pendulum System (FPS) and known in Europe as Curved Surface Sliders (CSSs). These isolation devices, available in different configurations (e.g. high damping rubber bearings, lead rubber bearings, CSS with single or multiple sliding surfaces, etc.) are equipped with inherent damping; their implementation results in lengthening of the first-mode period and in simultaneous increase of the energy dissipation capability of the isolated structure. Hence, a base-isolated structure undergoes low base shear and structural accelerations, and ideally behaves as a rigid body. However, the lateral flexibility of the isolation devices entails a large displacement demand, even of the order of 40-70 cm depending on the ground motion intensity and on the chosen fundamental period of the isolation system, as documented in manufacturers' datasheets [7]-[9]. This displacement demand is mainly accommodated by the isolation system, thereby requiring the use of large-size isolators. Moreover, large base displacements turn out to be an issue for nonstructural elements, lifelines and utilities crossing the joints between the superstructure and the surrounding ground (i.e. elevators, waterworks, gas fittings and electrical conduits in buildings, road joints in bridges), which must be flexible enough to tolerate the bearings' movement without failure. Finally, large isolators' displacements increase the risk of mutual collision or structural pounding between buildings, especially in densely populated areas [10]. Therefore, the development of practical solutions aimed at reducing the displacement demand of the isolation system is acknowledged to be a research topic with important practical repercussions.

To this aim, different strategies have been proposed to control isolator displacements. The most common approach would be to provide supplemental damping in addition to the inherent damping of the isolators, for instance by means of additional fluid viscous dampers or hysteretic dampers placed in parallel to the isolation system. However, while the supplemental damping does reduce the displacement demand, this is achieved at the expense of increasing the higher mode response as a counter effect, thus producing higher interstory drifts and floor accelerations in the superstructure [11]. Another strategy would be to design the isolation devices with increased stiffness at large displacements. This may be achieved in different ways: for instance, in elastomeric bearings via a strain-induced crystallization of the fillers [12], and in CSSs via a decrease in radius of curvature and/or an increase in friction coefficient close the edge of the sliding surface [13], [14]. In this context, sliding magnetic bearings have shown the benefits of adaptive energy dissipation and alterable deflection constraint by an elegant configuration design of isolation systems, as recently demonstrated experimentally [15] and through numerical studies [16], [17]. Another strategy would consist of a tuned mass damper (TMD) [18]-[20] or an inerter-based vibration absorber [21]-[23] placed immediately above or below the isolation floor, respectively, thus realizing a more robust hybrid control scheme.

Beside the displacement capacity $d_{\max}$, another fundamental property of the isolation system is the re-centering capability, i.e. the ability of recovering the original position at the end of the earthquake [24]. This capability is usually quantified via the residual displacement d_{res} after a seismic event [25]. A residual displacement from previous foreshocks not only affects the serviceability of the structure, but may also result in an increase of the isolator's displacement in case of aftershocks and future events [26]. In this regard, the friction coefficient of CSSs affects both the displacement demand and the re-centering capability of the isolation system [27]-[29]. Low-friction CSSs have a good re-centering behavior but undergo large displacement during extreme earthquakes because of the lower energy dissipation capability; on the contrary, high-friction CSSs are characterized by a lower displacement demand, but also by a poor re-centering behavior at low-intensity (serviceability-level) earthquakes. Another drawback of high-friction CSSs is related to the high static friction coefficient at breakaway, which can delay or even prevent engagement of sliding at the isolation interface especially under low-to-moderate intensity earthquakes [30].

Considering that energy dissipation and re-centering capability are two competing aspects of CSSs, and taking into account the different performance requirements depending on the intensity level of the seismic excitation, the goal for an optimal isolation strategy would be to obtain a good re-centering behavior for both serviceability and extreme earthquakes, ensured by a low friction coefficient of the CSSs that also minimizes breakaway effects, combined with a supplemental energy dissipation that is engaged during extreme earthquakes only. Such desired "displacement-dependent" dissipation capability can be accomplished by means of gap dampers [31]-[33], which provide supplemental energy dissipation only when the displacement of the CSS exceeds a threshold, called gap displacement d_{gap}, while not being engaged for smaller displacements. Additionally, the flag-shaped hysteresis of shape memory alloys (SMAs) has been recognized as a unique property in civil engineering applications [34]-[36] that can be conveniently exploited to develop efficient isolation systems [37]-[40], providing energy dissipation without implying residual displacements. Based on these motivations, an effective base-isolation layout that combines low-friction CSSs with a novel scheme of shape memory alloy gap dampers (SMAGDs) is developed in this paper. After describing the conceptual model of the SMAGD, a performance-oriented design procedure is developed based on displacement spectral analysis, by introducing some reasonable assumptions for the definition of the linear equivalent mechanical properties of the CSS+SMAGD combined isolation system and assuming a target displacement demand under the maximum credible design earthquake. The SMAGDs can be designed to provide a satisfactory energy dissipation without impairing the re-centering capability of low-friction CSSs. The proposed design method is validated against results from nonlinear response history analyses. Based on a wide parametric study comprising a variety of CSS and SMAGD properties, it is found that the proposed isolation layout is characterized by negligible residual displacement and absolute acceleration during weak "serviceability" earthquakes, due to the low friction coefficient of the CSSs, and by reduced displacement demand during extreme earthquakes, guaranteed by the supplemental stiffening and energy dissipation introduced by the SMAGD.

2. PRELIMINARY REMARKS ON THE HYSTERETIC BEHAVIOR OF CSS

Some preliminary remarks on the hysteretic behavior of the CSS are briefly recalled here. The force-displacement relation of a CSS isolation system can be analytically described by a bilinear hysteretic model as sketched in Figure 1. According to this model, the restoring force contribution F_r (governed

by the effective radius of curvature R_{eff}) and the friction force contribution F_f (that is independent from the displacement) add up, thus giving rise to the following expression of the total reaction force:

$$F = F_r + F_f = k_p d + F_0 \text{sgn}(\dot{d}) \tag{1}$$

where $F_0 = \mu_d \cdot N$ denotes the characteristic strength of the CSS, μ_d represents the dynamic friction coefficient, N is the vertical load acting on the bearing, $k_p = N/R_{\text{eff}}$ is the restoring stiffness, d and $\dot{d}$ indicate the horizontal displacement and velocity, respectively, and $sgn(\cdot)$ is the signum function. The dynamic friction coefficient μ_d is a leading factor for the hysteretic behavior of the CSS. For current thermoplastic sliding materials available on the market (e.g. PTFE, UHMWPE), it varies with the lubrication condition, the sliding velocity, the contact pressure and the temperature [41], [42]. Although complex models of the friction coefficient that depend upon contact pressure, sliding velocity and temperature at the sliding interface have been proposed in the literature [43]-[48], in this paper a simple velocity-dependent friction law is adopted, according to the exponential function [49]

$$\mu_d = \mu_{HV} - (\mu_{HV} - \mu_{LV}) \cdot \exp(\alpha \dot{d}) \tag{2}$$

where μ_{LV} and μ_{HV} represent the friction coefficients at low and high velocities, respectively, and α (having units of inverse of velocity) denotes a rate parameter governing the transition from μ_{LV} to μ_{HV}.

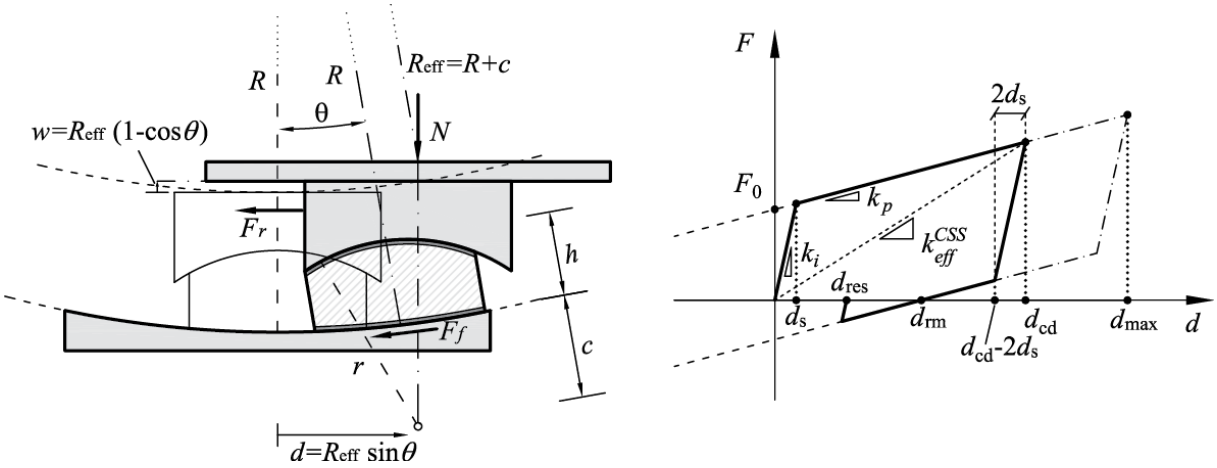

Figure 1 Kinematics and free body diagram of CSS (left) and idealized force-displacement relation (right)

The initial stiffness of the CSS (relevant to the pre-sliding phase) is typically very high, and can be set to $k_i \approx 100\, k_p$ [5], which also implies that the actual displacement at which sliding starts $d_{\text{s}} \cong F_0/(100\, N/R_{\text{eff}})$ is practically zero. The maximum static residual displacement d_{rm} can be identified by imposing that the two force contributions (restoring and frictional) balance one other, which leads to the following value [28]

$$d_{\text{rm}} = \mu_d \frac{N}{k_p} = \mu_d R_{\text{eff}} \,. \tag{3}$$

The value d_{rm} represents the upper bound of the actual residual displacement d_{res} at the end of the earthquake, i.e. $-d_{rm} < d_{\text{res}} < d_{\text{rm}}$. As shown by Eq. (3), the re-centering behavior of the CSS worsens as the dynamic friction coefficient μ_d and/or the effective radius of curvature R_{eff} increase. Consequently, CSS isolation systems having large d_{rm} values are susceptible to higher residual displacements, which means that the re-centering behavior is negatively affected by d_{rm}. On the

contrary, the energy dissipation capability of the CSS is positively affected by the value of d_{rm}, as can be noted by calculating the effective damping ξ_{d} for a cyclic motion characterized by an assigned displacement amplitude d_{cd}:

$$\xi_d = \frac{2}{\pi} \cdot \frac{\mu_d R_{\mathrm{eff}}}{\mu_d R_{\mathrm{eff}} + d_{\mathrm{cd}}} = \frac{2}{\pi} \cdot \frac{1}{1 + \left(\frac{d_{\mathrm{cd}}}{d_{\mathrm{rm}}}\right)} . \tag{4}$$

The previous observations reveal that re-centering capability and the energy dissipation are two competing aspects in CSSs. This circumstance motivates the development of alternative dissipation mechanisms that are not engaged throughout the range of displacements, in order to meet different performance criteria at various levels of the earthquake excitation. Such "displacement-dependent" damping mechanism is promoted in this paper to reduce the displacement demand of low-friction CSSs, without impairing their typical good re-centering capability. In the next Section, first a conventional realization scheme of hysteretic gap dampers proposed in the literature [32], [33] is described and critically analyzed in terms of its re-centering behavior. Then, a novel SMA-based gap damper (SMAGD) system is elaborated in order to optimize the re-centering capability of the combined CSS+SMAGD isolation layout.

3. GAP DAMPER SYSTEM

3.1. Conventional realization scheme of hysteretic gap dampers

A realization scheme and the corresponding force-displacement relationship of hysteretic gap dampers is illustrated in Figure 2. This scheme was previously studied from a conceptual, numerical and experimental point of view [31]-[33] with the main aim of reducing displacements of the isolation system during extreme events. CSS isolators are arranged in parallel with hysteretic gap dampers along the direction of motion. For simplicity, the real multi-directional nature of the earthquake ground motion is neglected in this feasibility study: assuming a unidirectional seismic excitation, two gap dampers are placed along the loading direction, one on the left side and one on the right side of the isolation nub. Based on this realization scheme, the CSSs provide the classical functions of the isolation system (e.g., support of the gravity loads from the superstructure, accommodation of lateral displacements with low stiffness, energy dissipation, re-centering capability), while the gap dampers introduce energy dissipation only when the displacement exceeds an assigned threshold, called gap displacement d_{gap}, while not being engaged otherwise. The ability of controlling the reaction force depending on the amplitude of the displacement is denoted as "phased behavior" in the literature [31]-[33]. Such phased behavior is achieved here by connecting the two gap dampers to the isolation system not directly, but through a rigid steel frame, whose lateral walls are separated from the central isolation nub at either side by a distance d_{gap}. Therefore, considering that the isolation nub is initially centered with respect to the rigid frame, the gap dampers are not engaged in the range of displacements $-d_{\mathrm{gap}} < d < d_{\mathrm{gap}}$. When an elastic-perfectly plastic behavior of the hysteretic gap damper is assumed (in both tension and compression) for displacements larger than d_{gap}, the step-by-step examination of the kinematics and the reaction force of the gap damper system is reported in Figure 2. In step 1, the gap dampers provide zero reaction force for displacements smaller than d_{gap} in either direction. In step 2, assuming a positive displacement $d_1 > d_{\mathrm{gap}}$ in the right direction, gap damper 1 (on the right side) and gap damper 2 (on the left side) are engaged in compression and in tension, respectively. The gap

damper now undergoes a permanent deformation d_{p1}, which causes a shift of the initial gap towards the right. This implies that, at motion reversal, only a portion of the total displacement d_1 is recovered, while the complementary portion d_{p1} is permanently accumulated.

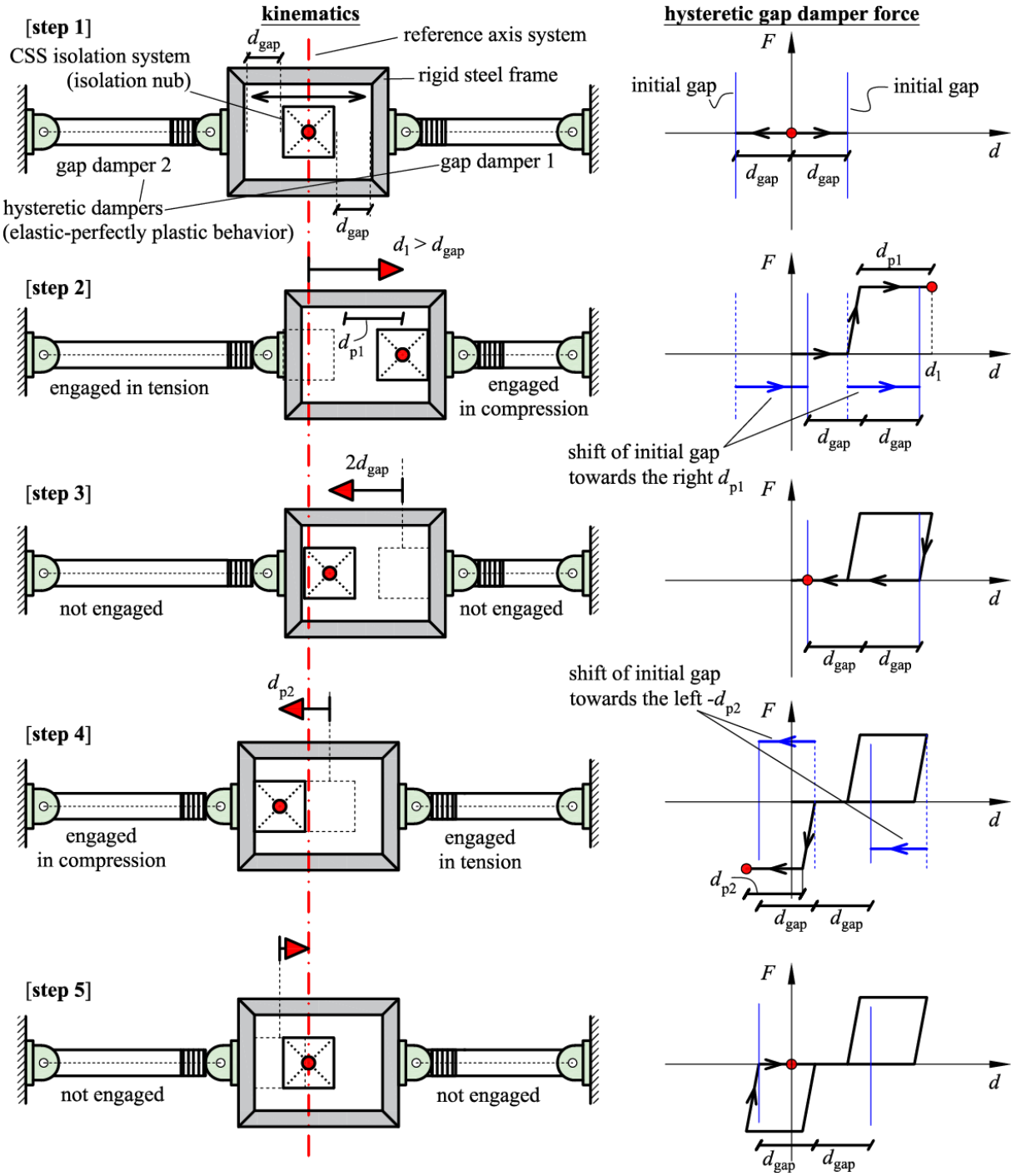

Figure 2 Conventional layout of isolation system with hysteretic gap dampers (scheme proposed in [32], [33])

In step 3, after moving leftward by a quantity $-2d_{gap}$, the isolation nub comes again into contact with the rigid frame and engages the gap dampers for a second time. However, the gap damper is now engaged not for a displacement $-d_{gap}$ with respect to the reference axis system (which was the initial gap in the original configuration), but for a displacement $d_{p1}-d_{gap}$. This means that, if the amount of

the permanent deformation of the gap damper along one direction is quite large, say $d_{\mathrm{p1}} > d_{\mathrm{gap}}$, the engagement of the gap damper system towards the opposite direction can even occur for displacements having the same sign, which is indeed the emblematic case represented in step 4 of Figure 2. In other words, the accumulation of permanent deformation of the hysteretic gap damper turns out to be detrimental for the re-centering behavior of the CSS isolation system, because when the isolation system tends to recover the initial undeformed position, the gap damper develops a nonzero reaction force that counteracts this re-centering behavior. In step 4, when moving leftwards, the system accumulates a permanent deformation d_{p2} in the negative direction, thus causing an overall shift of the initial gap of an overall quantity $d_{\mathrm{p1}} - d_{\mathrm{p2}}$ (positive rightward for the case in Figure 2, assuming $|d_{\mathrm{p1}}| > |d_{\mathrm{p2}}|$). Finally, in step 5 the isolation system returns to the origin.

Evidently, the above-described phenomenon of permanent shift of the initial gap during the response history may negatively affect the overall system performance, as was recognized in [33]. In particular, for asymmetric accelerograms such as pulse-like excitations with marked directivity effects, the cyclic motion of the isolation system could slow down in a configuration in which the rigid steel frame is shifted in one direction (e.g. towards the right as in the step 3 described above) and such permanent deformation may be quite large. In these circumstances, the restoring force of the CSS, F_r (cf. Eq. (1)) that acts to re-center the isolation system at the end of the shaking, would be counteracted by the reaction force of the gap damper system close to the origin of the displacement axis. Consequently, the shift of the initial gap, which is an inherent feature of this realization scheme of the gap damper system, may be detrimental for the re-centering behavior of the isolation system as a whole.

3.2. Alternative realization scheme of hysteretic gap dampers

An alternative realization scheme that does not impair the re-centering capability of the isolation system is illustrated in Figure 3. The seismic performance of this scheme was investigated in a recent research work by the authors [50]. Therefore, only a brief description is given here, which is preparatory for introducing the novel SMA-based gap damper system in the next subsection. Similar to the previous realization scheme shown in Figure 2, the layout in Figure 3 involves two hysteretic gap dampers that are placed at a distance d_{gap} from either side of the isolation system. However, the steel rigid frame surrounding the isolation nub is replaced by two independent steel walls, which represents the main difference between the two schemes. This configuration allows the engagement of one gap damper at a time, either gap damper 1 on the right-hand side or gap damper 2 on the left-hand side, depending on the actual direction of motion of the isolation system. Hence, the gap dampers are engaged as two "compression-only" elements. In order to gain a quick insight into the hysteretic behavior of this gap damper system, an imposed displacement time history consisting of three sinusoidal waves with increasing amplitude (d_1, d_2, d_3, respectively) is assumed, and the corresponding force-displacement relationship is plotted. Evidently, this realization scheme does not produce any reaction force in the neighborhood of the origin of the displacement axis, which ensures that the re-centering behavior of the isolation system is not altered, unlike the previous realization scheme. However, the main drawback of this layout is related to the effect of the permanent deformation on the displacement reduction capability of the gap damper system. More specifically, the engagement of each gap damper modifies the gap displacement and causes a permanent shift of the engagement point along the direction of motion – this effect was termed "cumulative damage" in the

previous work [49].

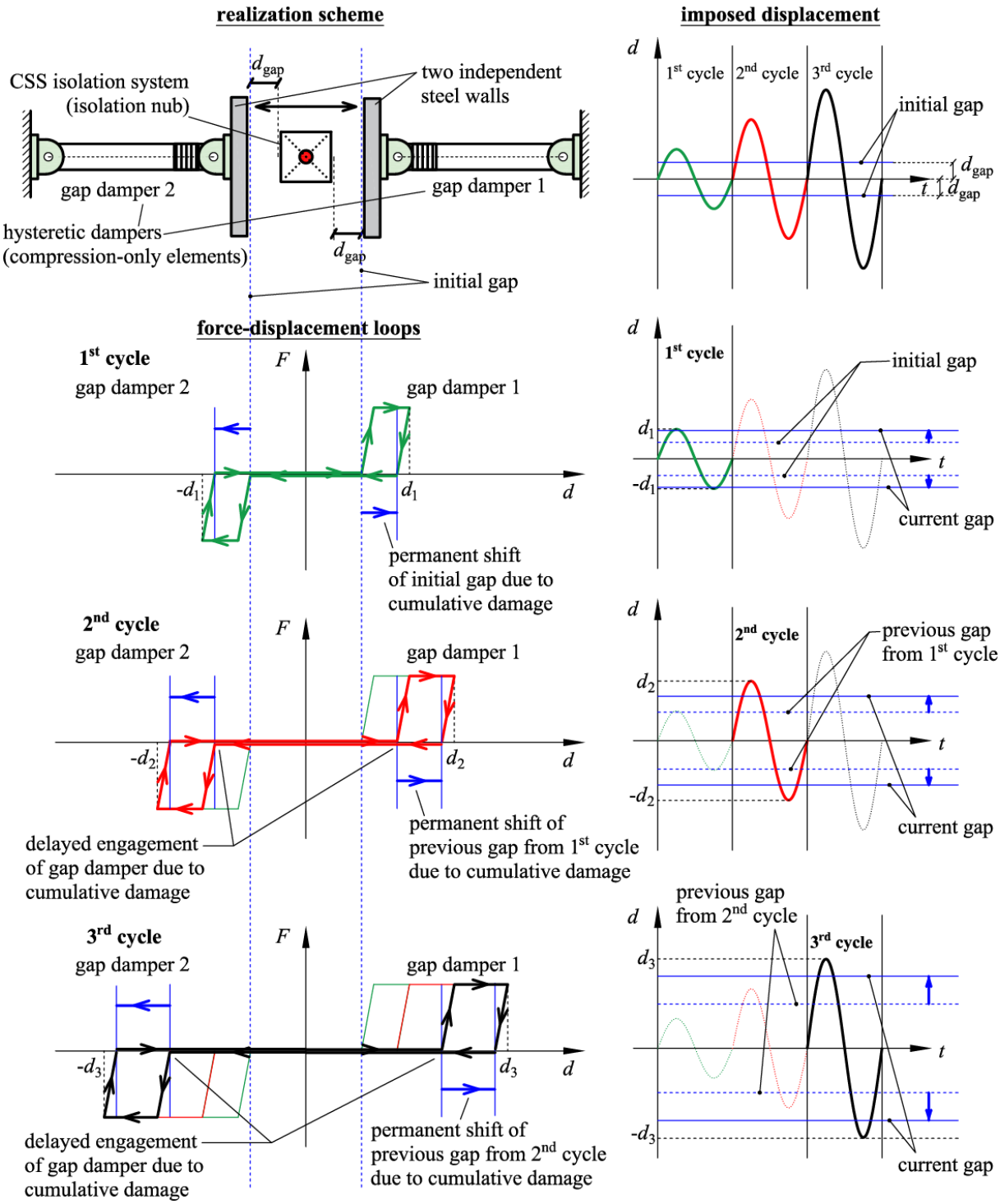

Figure 3 Alternative realization scheme [50] with two "compression-only" hysteretic gap dampers and effect of the cumulative damage during response history analysis

Because of such undesired cumulative damage, the gap interval $[-d_{\text{gap}}, d_{\text{gap}}]$ is not constant throughout the entire response history, but becomes wider at each gap damper engagement. As can be seen, during the second and third cycle the engagement of the gap damper is delayed due to the shift of the initial gap produced in the previous cycle(s); the displacement time history is purposely assumed with increasing amplitude in subsequent cycles to shed light on this issue. Consequently, the reduction

of the isolation displacement may not be effectively accomplished when the actual gap displacement is larger than the initial gap assumed in the design phase $[-d_{\text{gap}}, d_{\text{gap}}]$. Therefore, the cumulative damage can be an issue when a severe ground motion occurs after previous excitation, e.g. strong aftershocks following previous shock, or a main shock occurring after preshocks.

3.3. Proposed realization scheme of SMA gap dampers (SMAGDs)

As demonstrated in the previous subsection, the engagement of one gap damper at a time as a "compression-only" dissipative element does not impair the re-centering capability of the isolation system. Nevertheless, the cumulative damage induced by the plastic deformation accumulated by each hysteretic damper jeopardizes the performance of the gap damper system over repeated cycles. Obviously, such cumulative damage is ascribed to the hysteretic nature of the gap dampers. Based on these considerations, a novel realization scheme is proposed in this paper, which is based on the combination of a CSS isolation system in parallel with two shape memory alloy gap dampers (SMAGDs) being placed at the left and right side of the isolation nub. In practical cases, similar realization schemes combining isolation bearings with adaptive dampers were proposed for strategic buildings, in an attempt to meet stringent performance requirements at different levels of the earthquake excitation, e.g. at design basis earthquake (DBE) and at maximum considered earthquake (MCE). As an emblematic example, in Figure 4 the earthquake protection system designed by Maurer SE for the Great Mosque of Algiers is illustrated, which combines low-friction sliding pendulum bearings (3% friction) and adaptive hydraulic dampers, the latter offering an intense reaction force at MCE level only, while providing a modest reaction force at lower DBE level.

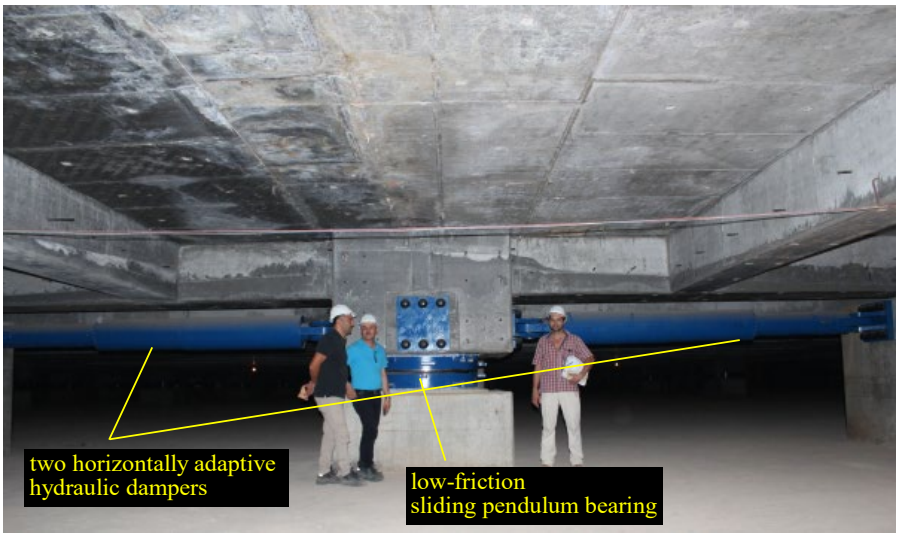

Figure 4 Protection system developed by Maurer SE for the Great Mosque of Algiers, combining sliding pendulum bearings and adaptive hydraulic dampers [Courtesy of http://structurae.net, image credits ID 276745]

Based on a similar realization scheme, the proposed isolation scheme combining low-friction CSS with SMAGDs is schematically illustrated in Figure 5. The SMAGD is a dissipative element that exploits the superelastic properties of SMAs, which can reduce or totally eliminate the aforementioned cumulative damage. Indeed, it is well known that the SMA constitutive model exhibits a flag-shaped hysteretic curve due to the reversible phase transformation from austenite to martensite and vice versa.

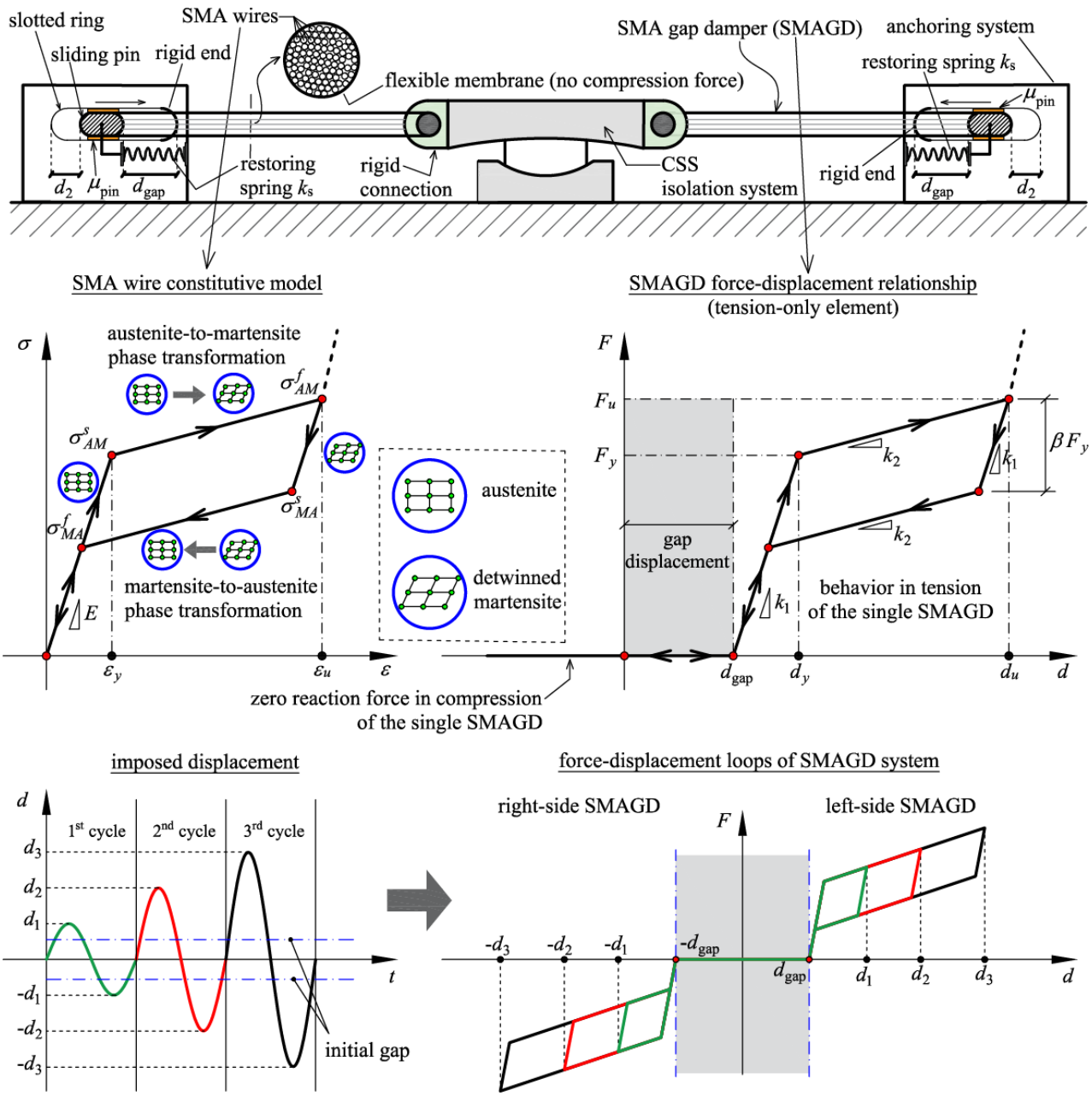

Figure 5 Proposed realization scheme of isolation system combined with two "tension-only" SMAGDs (top), SMA wire constitutive model and SMAGD force-displacement relationship (center), and response history analysis of SMAGD system under three sinusoidal displacement waves with increasing amplitude (bottom)

This allows the recovery of the original, undeformed shape upon unloading, as represented in the idealized stress-strain curve shown in the mid-left part of Figure 5, thus minimizing the residual strains (typically less than 1% [40]). In this figure, the material parameters and the corresponding physical meanings are as follows: E is the elastic modulus of both the austenite and martensite branches; σ^s_{AM} and σ^f_{AM} denote the stress levels at which austenite-to-martensite phase transformation starts and finishes, respectively, while ε_y and ε_u indicate the corresponding strain levels; σ^s_{MA} and σ^f_{MA} represent the stress levels at which martensite-to-austenite phase transformation starts and finishes, respectively. Typical values of maximum recoverable strain ε_u range from 6% to 8% [39] depending on the alloy characteristics.

In the proposed configuration of Figure 5, several aligned SMA wires are grouped together and confined within a flexible membrane to form the SMAGD. The total area of the SMA wires, denoted as A_{SMAGD} in the sequel of the manuscript, defines the cross section of the damper, which is directly related to the amount of damping force provided by the SMAGD. At one end the SMAGD is rigidly connected to the CSS, whereas at the opposite terminal it is connected to an anchoring system where a sliding pin and a slotted ring accomplish the "gap damper" feature and make the SMAGDs work as two "tension-only" damping elements. Indeed, the slot of the fixation ring is designed to accommodate displacements of the isolation nub up to a desired threshold d_{gap}, but for displacements $d > d_{\text{gap}}$ the motion of the sliding pin is constrained by the wall of the slotted ring (rigid end in Figure 5) and the SMAGD is stretched, thereby developing a tensile force. The anchoring system of the left-side SMAGD is symmetric to that of the right-side SMAGD in such a way that only one SMAGD at a time is engaged as "tension-only" element depending on the actual direction of motion of the isolation system, while the other SMAGD provides zero compression force. However, since the SMAGD works as a "tension-only" element, after one complete cycle of motion with amplitude $\geq d_{\text{gap}}$ both sliding pins would be in contact with the rigid ends of the slotted rings, and no gap would be left to accommodate future movements. Indeed, the SMAGD is capable to pull the pin towards the isolation nub only, while no other mechanism pushes the pin in the opposite direction to recover the gap at the motion reversal, hence the initial gap would be completely lost. To avoid this effect, a spring of length d_{gap} is installed at either anchoring system to provide a restoring force that pushes the sliding pin back to its initial position when it is no longer pulled by the SMAGD. The restoring spring stiffness k_s is assigned such that the corresponding force at the maximum deflection of the spring $F_{\text{spring}} = k_s \cdot d_{\text{gap}}$ is sufficient to overcome the friction force and the inertia force of the sliding pin, that is

$$F_{\text{spring}} = k_s \cdot d_{\text{gap}} \geq F_{\text{pin}}^{\text{friction}} + F_{\text{pin}}^{\text{inertia}} = \mu_{\text{pin}} \cdot m_{\text{pin}} \cdot \text{g} + m_{\text{pin}} \cdot \text{acc}_{\text{pin}} \tag{5}$$

Such condition can be rewritten as a design condition in terms of the restoring spring stiffness k_s as follows

$$k_s \geq m_{\text{pin}} \left(\frac{\mu_{pin} \cdot \text{g}}{d_{\text{gap}}} + \frac{\text{acc}_{\text{pin}}}{d_{\text{gap}}} \right). \tag{6}$$

By simple calculations, it is seen that a small spring force F_{spring} is sufficient to recover the gap. As an example, by assuming a friction coefficient of metal-to-metal contact $\mu_{\text{pin}} = 50\%$, a reasonable mass of the pin equal to 10 kg, and a (quite large) maximum acceleration of the pin equal to 0.5 g, the force resulting from Eq. (5) is around 0.1 kN. When the SMAGD is engaged in tension, the force of the spring system acts in the opposite direction, but since it is much lower than the reaction force of the SMAGD, it can be neglected in the calculations. As soon as the SMAGD is no longer in tension (i.e., after motion reversal), the spring k_s tends to restore the sliding pin back to the original position at a distance d_{gap} from the slot rigid wall, which is the only equilibrium position of the restoring spring system. Small oscillations about such equilibrium position are likely to occur, therefore in the opposite direction a certain gap d_2 is assigned in order to prevent bumps during the restoring movement of the sliding pin. Moreover, the force developed from the spring system is also beneficial to induce a small tension in the SMA wires and prevent their buckling when the motion of the isolation nub pushes the SMAGD away from the undeformed configuration. It is worth noting that this scheme is similar to that of the two "compression-only" hysteretic gap dampers (cf. Figure 3), but does not suffer from the

cumulative damage due to the superelastic behavior of SMAs.The idealized force-displacement relationship of each SMAGD is shown in the mid-right part of Figure 5 under the simplifying hypothesis of equal slope k_2 in the austenite-to-martensite and in martensite-to-austenite phase transformation branches – this is a reasonable assumption considering typical experimental properties observed in commercially available alloys, such as NiTi [34], [39]. In this figure, d_y and d_u denote the displacements at which the austenite to martensite phase transformation starts and finishes, respectively. Once the material parameters of the SMA wires are defined as above, the corresponding parameters reported in Figure 5 that define the force-displacement relationship of the SMAGD can be computed as follows

$$F_y = \sigma_{AM}^{s} \cdot A_{SMA};\ F_u = \sigma_{AM}^{f} \cdot A_{SMA};\ d_y = d_{\text{gap}} + \varepsilon_y L_{SMAGD};\ d_u = d_{\text{gap}} + \varepsilon_u L_{SMAGD}$$
$$k_1 = \frac{E \cdot A_{SMA}}{L_{SMAGD}};\ k_2 = \frac{F_u - F_y}{d_u - d_y} = \left(\frac{\sigma_{AM}^{f} - \sigma_{AM}^{s}}{\varepsilon_u - \varepsilon_y}\right) \cdot \left(\frac{A_{SMA}}{L_{SMAGD}}\right);\ \beta = \frac{\sigma_{AM}^{f} - \sigma_{MA}^{s}}{\sigma_{AM}^{s}} = 1 - \frac{\sigma_{MA}^{f}}{\sigma_{AM}^{s}} \tag{7}$$

where L_{SMAGD} indicates the length of the SMA wires, while the two expressions of β are equal to each other because of the assumption of equal slope k_2 in the loading and unloading branches. Note that the force transferred by the spring system in Figure 5 F_{spring} , is very small in comparison to F_y, therefore in the force-displacement relationship of the SMAGD this small pretensioning force can be practically ignored. In order to enlighten the advantages of the superelastic behavior and the elimination of the cumulative damage exhibited by the hysteretic gap dampers over repeated cycles, the response history analysis under three sinusoidal displacement waves with increasing amplitude (as previously considered for the hysteretic gap dampers in Figure 3) is analyzed in the bottom part of Figure 5. Evidently, the SMAGD is ideally engaged at the same gap displacement d_{gap} at each cycle, irrespective of the previous response history, and its flag-shaped behavior without permanent deformation is particularly suitable for reducing the displacement demand of the isolation system.

The idealized hysteretic behavior of CSS (with constant friction), SMAGD, and the combined CSS+SMAGD system is depicted in Figure 6. In particular, the flag-shaped hysteresis of the SMAGD combined with the bilinear hysteretic model of the CSS gives rise to a piecewise hysteretic model. During minor earthquakes ($d \leq d_{\text{gap}}$) the overall resisting force is provided by the CSS only, whereas during severe excitations ($d > d_{\text{gap}}$) the SMAGD system is engaged. In particular, the SMAGD introduces two beneficial effects, namely an increase of stiffness of the overall system at large displacements, and secondarily an increase in damping. In order to compute the actual contribution provided by the SMAGD in terms of both stiffening effect and damping force, the displacement and force values of the 9 characteristic points identifying the force-displacement loop of the combined CSS+SMAGD system are listed in Table 1 – only the positive branch is considered for symmetry reasons. As an example, the branch from P_2 to P_3 (from displacement d_{gap} to d_y) has stiffness $k_p + k_1$, while the branch from P_3 to P_4 (from displacement d_y to d_{max}) has stiffness $k_p + k_2$. This demonstrates how the stiffness parameters k_1 and k_2 of SMAGDs sum up to the stiffness of the CSS, k_p, in order to increase the overall stiffness of the combined CSS+SMAGD system.

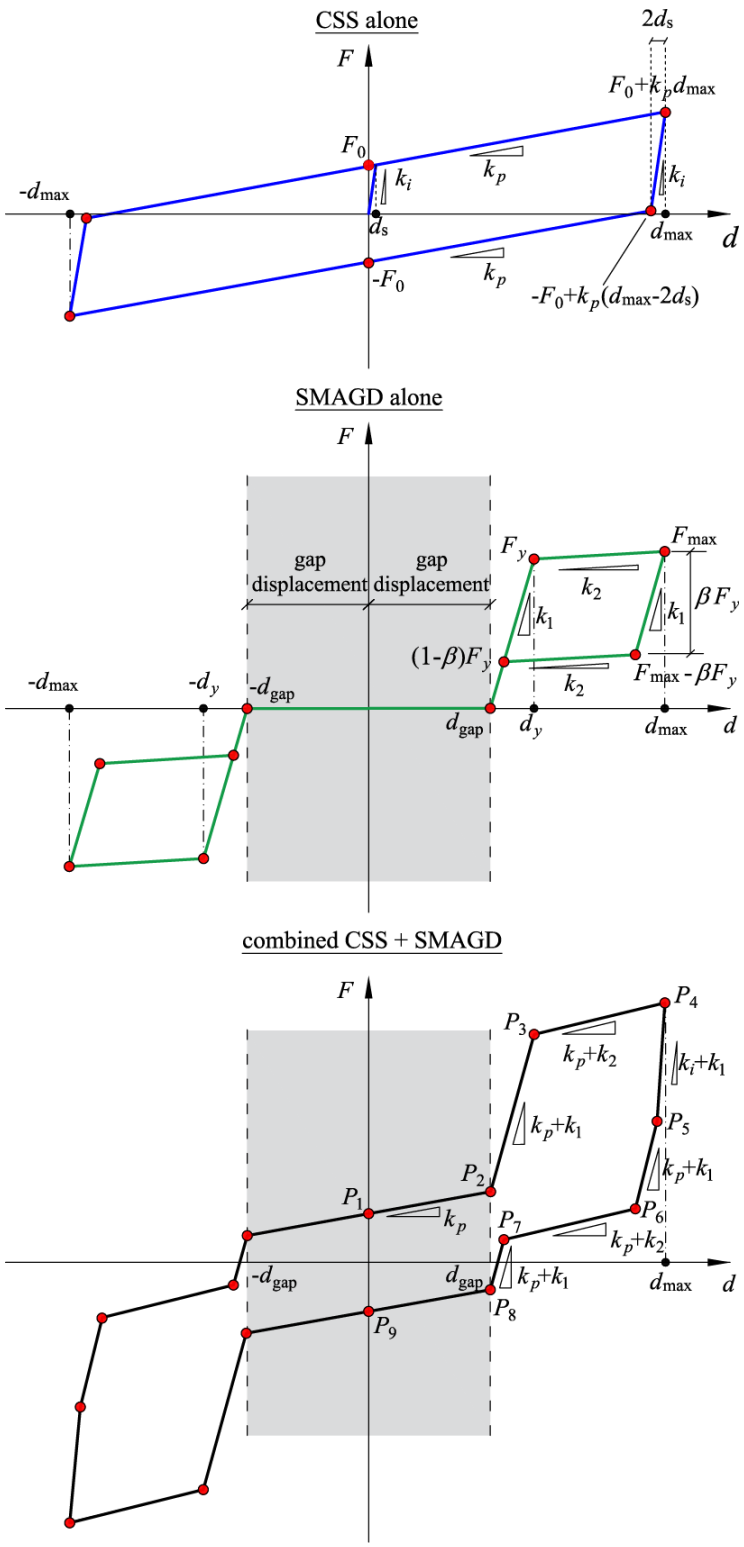

Figure 6 Hysteretic behavior of CSS (top), SMAGD (center) and combined CSS+SMAGD system (bottom)

In order to guarantee a good re-centering behavior of the combined system (and, simultaneously, to avoid breakaway effects induced by high static friction coefficients), the CSS isolators should be preferably equipped with a low-friction sliding material, while the phased behavior of the SMAGD generates supplemental stiffening and damping in order to keep peak displacements to within a desired threshold. A design procedure to select the parameters of the SMAGD in the combined CSS+SMAGD

system is presented in the next Section. Furthermore, this combined system overcomes the inherent issue of high-friction CSSs that suffer from poor re-centering capability and high absolute peak accelerations at low-intensity ground motions [29]. The latter effect is particularly important for "acceleration-sensitive" non-structural elements whose protection is an important target, especially during minor frequent earthquakes [51].

Table 1 Characteristic points of the CSS+SMAGD ideal hysteretic cycle

Point	Displacement d	Force F
P_1	$P_{1d} = 0$	$P_{1F} = F_0$
P_2	$P_{2d} = d_{\text{gap}}$	$P_{2F} = F_0 + k_p d_{\text{gap}}$
P_3	$P_{3d} = d_y$	$P_{3F} = P_{2F} + (k_p + k_1)\left(d_y - d_{\text{gap}}\right)$
P_4	$P_{4d} = d_{\max}$	$P_{4F} = F_0 + k_p d_{\max} + F_{\max}$ †
P_5	$P_{5d} = d_{\max} - 2d_s$	$P_{5F} = P_{4F} - (k_i + k_1)2\ d_s$
P_6	$P_{6d} = d_{\max} - \beta F_y / k_1$	$P_{6F} = P_{5F} - (P_{5d} - P_{6d})(k_p + k_1)$
P_7	$P_{7d} = d_{\text{gap}} + (1-\beta) F_y / k_1$	$P_{7F} = P_{6F} - (P_{6d} - P_{7d})(k_p + k_2)$
P_8	$P_{8d} = d_{\text{gap}}$	$P_{8F} = k_p d_{\text{gap}} - F_0$
P_9	$P_{9d} = 0$	$P_{9F} = -F_0$

† $F_{\max} = F_y + k_2\left(d_{\max} - d_y\right)$

4. LINEAR PROCEDURE FOR PRELIMINARY ANALYSIS AND DESIGN

The response spectrum method is a popular approach for designing base isolation systems, at least as a preliminary tool to obtain an estimate of the maximum response of isolated structures avoiding more computationally expensive nonlinear response history analyses (NLRHAs) [52]. Based on the response spectrum principles, a linear procedure for the preliminary design of structures equipped with the proposed CSS+SMAGD system is developed here. The procedure assumes that the base-isolated structure can be modeled as a single degree of freedom (SDOF) system, postulating a rigid-body behavior for the superstructure. In particular, the procedure is aimed at achieving a target displacement demand of the combined CSS+SMAGD system under the maximum credible design earthquake. To this end, displacement spectral analysis is carried out, introducing some reasonable assumptions for the definition of the linear equivalent mechanical properties of CSS, SMAGD and combined CSS+SMAGD system. Since equivalent mechanical properties inherently depend on the displacement response due to the nonlinear behavior of the devices, the determination of such parameters is carried out iteratively until convergence is reached. Key design parameters are the overall cross-sectional area A_{SMAGD} and the length L_{SMAGD} of the SMA wires in the SMAGDs. The overall cross-sectional area A_{SMAGD}, according to the expressions reported in (7), is directly related to the amount of damping force (F_y, F_u values) and to the stiffness contribution (k_1, k_2 coefficients) provided by the SMAGD. Therefore, A_{SMAGD} affects both the effective stiffness k_{eff} and the equivalent viscous damping ξ_{eff} of the combined CSS+SMAGD system. Similarly, the length of the SMA wires L_{SMAGD} influences the stiffness of the SMAGD, its yield displacement d_y (hence the ductility factor and the related damping properties), and the ultimate displacement d_u below which the SMAGD exhibits superelastic behavior. For displacements $d > d_u$ the reversible austenite to martensite phase transformation is completed, therefore displacements exceeding this threshold will not be entirely recovered upon unloading. In the next two subsections the main expressions and underlying assumptions of the linear procedure are presented, while in the following subsection 5.3 the procedure is validated against results from

NLRHAs for a variety of parameters of both CSS isolation system and SMAGD.

4.1. Iterative displacement spectral analysis

As sketched in the top part of Figure 5, the proposed isolation layout is composed of two subsystems acting in parallel, namely CSS and SMAGD. The parameters defining the dynamic behavior of the CSS isolation system are the effective radius of curvature R_{eff} and the dynamic friction coefficient μ_d; on the other hand, the parameters defining the dynamic behavior of the SMAGD are the gap displacement d_{gap}, the geometric parameters of the SMAGD, namely the total area of the SMA wires A_{SMA} defining the damper cross section, the length of the SMA wires L_{SMAGD}, and the material properties defining the constitutive model of the SMA $E, \sigma_{AM}^{s}, \sigma_{AM}^{f}, \sigma_{MA}^{s}, \sigma_{MA}^{f}, \varepsilon_y, \varepsilon_u$, whose physical meaning was previously illustrated in the mid-left part of Figure 5.

In a design phase, the nonlinear behavior of the two subsystems CSS and SMAGD is linearized in terms of effective stiffness k_{eff}^{CSS}, k_{eff}^{SMAGD} and equivalent viscous damping $\xi_{eff}^{CSS}, \xi_{eff}^{SMAGD}$, respectively. Considering the two subsystems acting in parallel, the fundamental period of the combined CSS+SMAGD system is

$$T_{eff} = 2\pi\sqrt{M/\left(k_{eff}^{CSS} + k_{eff}^{SMAGD}\right)} \tag{8}$$

where M denotes the overall mass of the base-isolated structure, including the base mass and the superstructure mass. On the other hand, the equivalent viscous damping of the combined CSS+SMAGD system is calculated, in accordance with the principles of the displacement-based seismic design of structures [53] involving parallel systems [54], as the weighted average with respect to the energy dissipated by each of the two subsystems (cf. the hysteretic behavior in Figure 6)

$$\xi_{eff} = \frac{\xi_{eff}^{CSS}\,(F_0\,d_{\max}) + \xi_{eff}^{SMAGD}\,(\beta\,F_y)\,(d_{\max} - d_{\text{gap}})}{F_0\,d_{\max} + (\beta\,F_y)\,(d_{\max} - d_{\text{gap}})}\,. \tag{9}$$

Based on expressions (8) and (9), the maximum displacement experienced by the system under the design earthquake can be estimated via the displacement response spectrum $d_{max} = S_d\left(T_{eff}, \xi_{eff}\right)$. However, since the linear equivalent mechanical properties T_{eff} and ξ_{eff} implicitly depend on the sought maximum displacement d_{max}, the value of the spectral displacement obtained from the response spectrum $S_{\text{d}}\left(T_{eff}, \xi_{eff}\right)$ could be different from the value of $d_{\max}$ assumed in the calculation of the pair (T_{eff}, ξ_{eff}). According to the procedure sketched in Figure 7, the determination of the maximum displacement must be performed iteratively starting from an initial trial displacement value: at a given step, the values of $(T_{eff}^{(i-1)}, \xi_{eff}^{(i-1)})$ are used to compute a spectral displacement $d_{\max}^{(i-1)} = S_{\text{d}}(T_{eff}^{(i-1)}, \xi_{eff}^{(i-1)})$; the latter displacement, when introduced in Eqns. (8) and (9), gives rise to a new pair of values $(T_{eff}^{(i)}, \xi_{eff}^{(i)})$ and, thus, to a new spectral displacement $d_{\max}^{(i)} = S_{\text{d}}(T_{eff}^{(i)}, \xi_{eff}^{(i)})$. The procedure is repeated cyclically until convergence is reached, i.e., $\left|d_{\max}^{(i)} - d_{\max}^{(i-1)}\right| \leq tol$, with tol being a small enough tolerance parameter.

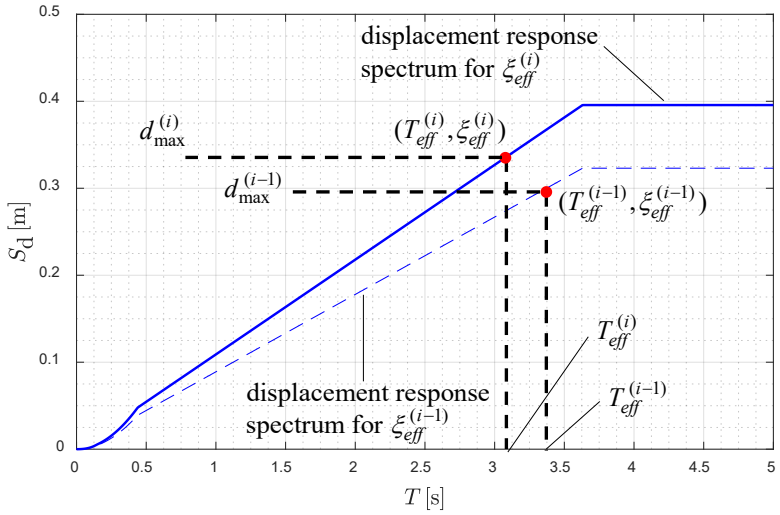

Figure 7 Iterative spectral analysis to compute the displacement demand of the combined CSS+SMAGD system

4.2. Linear equivalent mechanical properties

The application of the iterative spectral displacement analysis described in the previous subsection implies the knowledge of the linear equivalent mechanical properties of the two subsystems, namely k_{eff}^{CSS}, k_{eff}^{SMAGD} and $\xi_{eff}^{CSS}, \xi_{eff}^{SMAGD}$. With regard to the effective stiffness parameters, it is necessary to focus on the force-displacement relationships of the two subsystems, while, with regard to the equivalent viscous damping ratios, semi-empirical expressions proposed in the literature for application to direct displacement-based design are adopted. These expressions were evaluated by minimizing the errors between NLRHAs and the equivalent linear system displacements [55].

For the CSS isolation system, the effective stiffness k_{eff}^{CSS} can be calculated as the peak-to-peak secant slope. Considering the bilinear hysteretic model represented in Figure 1 and the governing resisting force expression (1), the effective stiffness is given by

$$k_{eff}^{CSS} = F_0/d_{\max} + N/R_{\text{eff}} \tag{10}$$

in which, it can be assumed $F_0 \cong \mu_{HV} \cdot N$ because in the cycle involving the maximum displacement, occurring during the strong motion phase of the accelerogram, the characteristic strength is reasonably governed by the high-velocity friction coefficient. On the other hand, the equivalent viscous damping of the CSS can be calculated with the formula proposed by Dwairi et al. [55] for elasto-plastic hysteretic systems

$$\begin{cases} \xi_{eff}^{CSS} = \left[85 + 60(1 - T_{eff})\right]\left(\frac{\mu_\Delta^{CSS} - 1}{\pi \mu_\Delta^{CSS}}\right) & T_{eff} < 1{,}0s \\ \xi_{eff}^{CSS} = 85\left(\frac{\mu_\Delta^{CSS} - 1}{\pi \mu_\Delta^{CSS}}\right) & T_{eff} \geq 1{,}0s \end{cases} \tag{11}$$

where T_{eff} denotes the effective fundamental period of the combined CSS+SMAGD system, and $\mu_\Delta^{CSS} = d_{\max}/d_s \cong 100\, d_{\max}/(\mu_{HV}\, R_{\text{eff}})$ indicates the ductility factor of the CSS (cf. again Figure 1). The proposed expression for the estimation of the equivalent viscous damping of CSS isolators overcomes the inherent problem of alternative approaches based on the Jacobsen formulation [56] that typically overestimate the energy-dissipation capacity of medium-to-long period hysteretic structures [54], such as base-isolated structures. Indeed, in all CSSs considered in this study, the equivalent

viscous damping calculated with the proposed formula ranges from 20% to 28%, while the Jacobsen approach would lead to much higher values of around 40-45%.

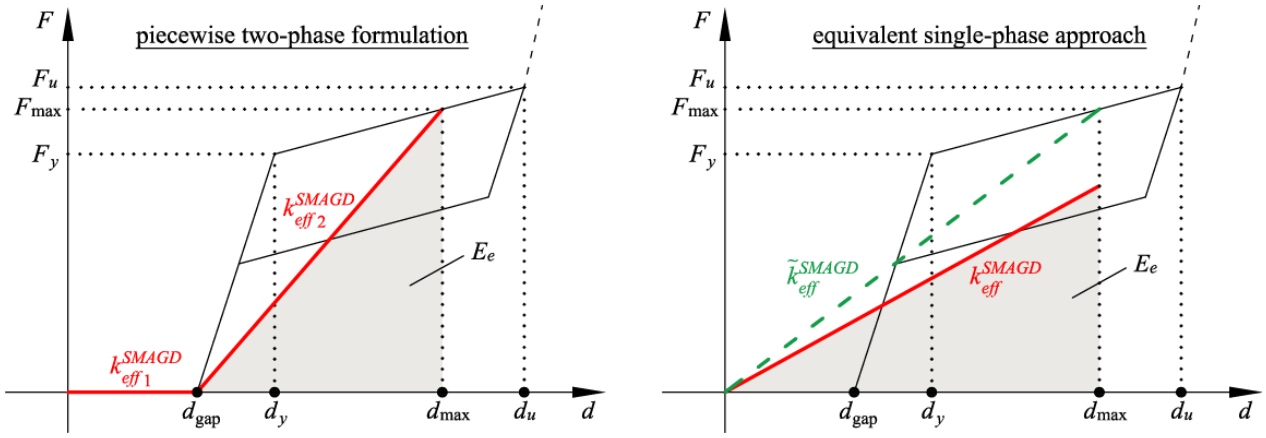

Figure 8 Determination of SMAGD effective stiffness: piecewise two-phase formulation (left) and equivalent single-phase continuous approach (right)

For the SMAGD, the determination of the effective stiffness should incorporate the effect of the gap displacement. Strictly speaking, referring to the sketch in the left side of Figure 8, the actual effective stiffness (secant slope) of the SMAGD would be obtained considering a piecewise "two-phase" behavior resulting in the following conditional expression

$$k_{eff}^{SMAGD} = \begin{cases} k_{eff1}^{SMAGD} = 0 & 0 \le |d| < d_{\text{gap}} \\ k_{eff2}^{SMAGD} = \dfrac{F_{\max}}{(d_{\max} - d_{\text{gap}})} & d_{\text{gap}} \le |d| \le d_{\max} \end{cases} \tag{12}$$

However, since spectral analyses require a linear continuous formulation for the effective stiffness throughout the range of displacements $0 \le |d| < d_{\max}$, the above two-phase approach is not suitable for the present study. To overcome this issue, an equal-elastic-energy criterion is here adopted in order to define an equivalent value k_{eff}^{SMAGD} of the SMAGD effective stiffness (right side of Figure 8). By assuming that the elastic energy E_e stored in the "two-phase" formulation is equal to the elastic energy stored in the equivalent "single-phase continuous" approach, an approximated value of the effective stiffness k_{eff}^{SMAGD} of the SMAGD can be derived as follows

$$k_{eff}^{SMAGD} = k_{eff2}^{SMAGD} \frac{(d_{\max} - d_{\text{gap}})^2}{(d_{\max})^2} = \frac{F_{\max}\,(d_{\max} - d_{\text{gap}})}{(d_{\max})^2}. \tag{13}$$

In traditional approaches, the effective stiffness would be identified by the green dashed line shown in the right panel of Figure 8, i.e. $\tilde{k}_{eff}^{SMAGD} = F_{\max}/d_{\max}$. Although such definition of the secant stiffness is consistent in terms of forces, it overestimates the elastic energy stored by the SMAGD due to the initial gap, thus leading to wrong predictions in terms of maximum displacements compared to NLRHAs (as verified by the authors). For this reason, the equal-elastic-energy criterion underlying Eq. (13) is adopted in the linear procedure, showing a much better accuracy as demonstrated in the sequel of the paper.

On the other hand, the equivalent viscous damping of the SMAGD can be calculated with the formula proposed by Dwairi et al. [55] for flag-shaped hysteretic systems

$$\begin{cases} \xi_{eff}^{SMAGD} = \left[30 + 35(1 - T_{eff})\right]\left(\frac{\mu_{\Delta}^{SMAGD}-1}{\pi\mu_{\Delta}^{SMAGD}}\right) & T_{eff} < 1{,}0s \\ \xi_{eff}^{SMAGD} = 30\left(\frac{\mu_{\Delta}^{SMAGD}-1}{\pi\mu_{\Delta}^{SMAGD}}\right) & T_{eff} \geq 1{,}0s \end{cases} \quad (14)$$

where T_{eff} denotes the effective fundamental period of the combined CSS+SMAGD system, while μ_{Δ}^{SMAGD} indicates the ductility factor of the SMAGD that, due to the presence of the gap, can be determined as follows

$$\mu_{\Delta}^{SMAGD} = \left(d_{\max} - d_{\text{gap}}\right)/\left(d_y - d_{\text{gap}}\right). \quad (15)$$

A validation of the proposed calculation method and the underlying assumptions for both k_{eff}^{SMAGD} and ξ_{eff}^{SMAGD} will be provided hereafter (subsection 5.3) by comparison with results from NLRHAs for a wide variety of system parameters. The SMAGD plays a fundamental role in the reduction of the isolators' displacements mainly thanks to its stiffening effect (period reduction), while the damping increase provides a minor (although not negligible) contribution. Indeed, in all the cases considered in this study, ξ_{eff}^{SMAGD} ranges between 5% and 10%, thus providing a lower energy dissipation contribution compared to CSS isolators.

5. NUMERICAL ANALYSES

A series of NLRHAs are performed to validate the design procedure developed in the previous section and to assess the seismic performance of the proposed CSS+SMAGD combined isolation system. A rigid-body behavior of the superstructure is postulated; hence the seismic response is examined through a simplified SDOF system. The seismic input consists of a suite of unidirectional historically recorded acceleration time histories. The structural analysis software program OpenSees v. 2.5.4 [57] is used to carry out NLRHAs. The CSS isolation system is modeled using a "Single Friction Pendulum Bearing Element" [58], with a velocity-dependent friction model governed by Eq. (2). The influence of the vertical component of the earthquake excitation is neglected. Therefore, a constant value of the vertical weight $N = 1000$ kN is assumed in the analyses to compute the mass of the isolation system as well as the CSS restoring stiffness k_p. On the other hand, the hysteretic behavior of the SMAGD is modeled through a "Series Material" composed of an "Elastic-Perfectly Plastic Gap Material" in series with a "SelfCentering Material" [58]. In the series material, stresses are equal and strains and flexibilities are additive. The parameters of the gap material are set in order to make the relevant series element to provide a null resisting force until the gap displacement d_{gap} is reached, and then to behave as a rigid link. Therefore, modulus of elasticity and yield stress of the gap material are assigned to a very high value (100 times higher than the corresponding values of the SelfCentering material) to simulate a realistic estimate of the impact force and to avoid yielding in the gap element. Although the SelfCentering Material is primarily used to model a self-centering energy-dissipative (SCED) brace [59], [60], in this paper it simulates the behavior of the SMA, whose characteristic parameters have been already discussed in Section 3.3 and are represented in Figure 5 (center-left).

5.1. CSS and SMAGD parameters

The goal is to compare the seismic performance of the conventional CSS isolation system against the proposed base isolation layout combining low-friction CSSs with SMAGDs. In this study, a reasonable range of CSS devices available on the market is considered, by including different radii of

curvature and different friction coefficients of the sliding material. In particular, three values of the effective radius of curvature (R_1, R_2, R_3), corresponding to CSS restoring periods $T = 2\pi\sqrt{R/g}$ equal to 2.98, 3.75, 4.49 s, and three friction classes (f_1, f_2, f_3), representative of low friction (LF), moderate friction (MF), and high-friction (HF) sliding materials are included in this study (Table 2). According to previous literature studies [26], [29], a constant ratio of high-velocity to low-velocity friction coefficient $\mu_{HV}/\mu_{LV} = 2.5$ is assumed for the three friction classes, and the rate parameter α governing the transition between the two friction values is set to $\alpha = 0.0055\ \mathrm{s/mm}$. The nomenclature adopted to identify the CSS isolation system is $R_i f_j$ (with $i = 1,2,3$ denoting the three curvature radii, and $j = 1,2,3$ denoting the three friction classes), which represents 9 combinations of parameters.

Table 2 CSS mechanical properties considered in this paper

Effective radius of curvature R_{eff}			Friction coefficient (μ_{LV}, μ_{HV})		
R_1 [mm]	R_2 [mm]	R_3 [mm]	f_1	f_2	f_3
2200	3500	5000	(0.02,0.05)	(0.035,0.0875)	(0.05,0.125)

With regard to the mechanical properties of the SMAGDs, two commercially available alloys are considered, namely NDC NiTi and GAC NiTi (NDC and GAC being the names of the manufacturing companies), whose material parameters were experimentally reported in [34] and are listed in Table 3. Both types of alloys are available in commercial superelastic NiTi straight wires, with circular cross section of 1.49 diameter and rectangular cross section of dimensions $0.64 \times 0.46\ \mathrm{mm}^2$, respectively [39]. The former alloy exhibits a hardening behavior ($k_2 > 0$), while the latter exhibits a perfectly plastic behavior ($k_2 = 0$), see the corresponding stress-strain laws in Figure 9. Note that the value of σ_{MA}^{s} in the NDC NiTi alloy (280 MPa) has been slightly changed in comparison with the original value (240 MPa) to meet the simplifying assumption of equal slope in the loading and unloading branches, which is consistent with the "SelfCentering Material" model in OpenSees [58].

Table 3 SMA material properties considered in this paper – experimental data taken from [39]

NDC NiTi		GAC NiTi	
E [MPa]	60000	E [MPa]	47000
σ_{AM}^{s} [MPa]	520	σ_{AM}^{s} [MPa]	350
σ_{AM}^{f} [MPa]	600	σ_{AM}^{f} [MPa]	350
σ_{MA}^{s} [MPa]	280†	σ_{MA}^{s} [MPa]	125
σ_{MA}^{f} [MPa]	200	σ_{MA}^{f} [MPa]	125
ε_y [%]	0.867	ε_y [%]	0.745
ε_u [%]	8	ε_u [%]	8

† assumed value to meet the assumption of equal slope k_2 in the loading and unloading branches

The length of the SMA wires is set to $L_{SMAGD} = 2000$ mm for the numerical examples, in order to keep the ultimate displacement of the SMAGD $d_u = d_{\mathrm{gap}} + \varepsilon_u L_{SMAGD}$ quite large. Indeed, displacements $d > d_u$ should be avoided because the SMAGD would lose its superelastic behavior: this is due to the fact the maximum recoverable strain ε_u of the SMA wire would be exceeded. The gap displacement is set to $d_{\mathrm{gap}} = 50$ mm and $d_{\mathrm{gap}} = 100$ mm in the validation of the design procedure, and $d_{\mathrm{gap}} = 50$ mm in the parametric study (motivations for these values will be given in the next subsections). Different values of A_{SMAGD} will be analyzed in the NLRHAs, as described in the

sequel of the paper.

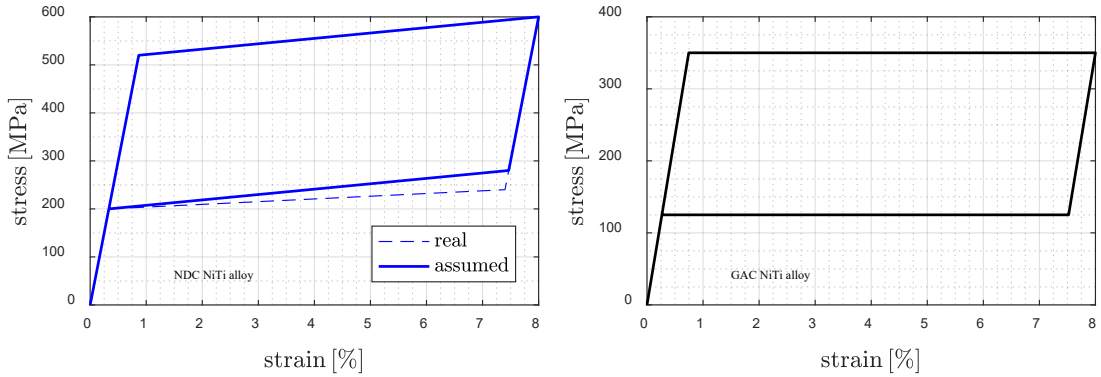

Figure 9 Uniaxial tension stress-strain curve of NDC NiTi alloy (left) and GAC NiTi alloy (right)

5.2. Ground motion selection and response of CSS isolation system

It is assumed that the proposed base isolation layout is placed in Lamezia Terme, Italy (latitude 38.57°, longitude 16.18°), where the seismic hazard map is provided by the Italian building code NTC2018 [61]. The following parameters are assumed for the definition of the design response spectrum: nominal life $V_N = 100$ years, functional class IV (amplification factor $C_U = 2.0$) and resulting reference life $V_R = V_N \cdot C_U = 200$ years. In accordance with the performance-based design principles, two distinct limit states are considered depending on the intensity level of the earthquake excitation. These two limit states are abbreviated as "SLD" and "SLC" in the Italian building code [61]: the former denotes a low-intensity serviceability earthquake with damage-limitation requirement and a 63% probability of exceedance during V_R (return period of 201 years), the latter denotes a maximum credible earthquake with no-collapse requirement and a 5% probability of exceedance during V_R (return period of 2475 years). A topography condition T_1 and a soil type A are assumed, which results in a peak ground acceleration (PGA) for the chosen installation site of 0.498 g and 0.181 g for SLC and SLD, respectively. For each limit state, a suite of seven independent spectrum-compatible historically recorded acceleration time histories are selected by means of the software REXEL v. 3.5 [62] from the European strong-motion database [63] among earthquakes with magnitude $6 \leq M_w \leq 7$ for SLC, and $5.5 \leq M_w \leq 6$ for SLD. The epicentral distance is set to $R_{ep} \leq 30$ km for both limit states. The spectrum-matching criterion is enforced in the range $[0.15 - 4.00]$ s, with an acceptable lower and upped tolerance of 10%. The recorded acceleration time histories are multiplied in magnitude by a scale factor (SF) in order to match the target acceleration response spectrum at 5% damping level. Seismological details of the selected ground motions are listed in Table 4 and Table 5 for SLD and SLC, respectively. A comparison between the target response spectrum and the median response spectrum computed from the seven selected records for each limit state is shown in Figure 10.

Table 4 Ground motion records selected for seismic analyses at SLD

Waveform ID (component)	Earthquake	Station ID	Date	M_w	R_{ep} [km]	PGA [g]	SF	scaled PGA [g]
5272 (x)	Mt. Vatnafjoll	ST2487	25/05/1987	6.0	24	0.033	5.51	0.181
368 (x)	Lazio Abruzzo	ST143	07/05/1984	5.9	22	0.064	2.82	0.181
1891 (y)	Kranidia	ST1320	25/10/1984	5.5	23	0.026	6.95	0.181
5270 (x)	Mt. Vatnafjoll	ST2486	25/05/1987	6.0	25	0.031	5.87	0.181
646 (y)	Umbria Marche	ST234	14/10/1997	5.6	17	0.029	6.35	0.181
642 (x)	Umbria Marche	ST225	14/10/1997	5.6	23	0.053	3.39	0.181
410 (y)	Golbasi	ST161	05/05/1986	6.0	29	0.055	3.30	0.181
			mean	**5.8**	**23.3**	**0.0415**	**4.88**	**0.181**

Table 5 Ground motion records selected for seismic analyses at SLC

Waveform ID (component)	Earthquake	Station ID	Date	M_w	R_{ep} [km]	PGA [g]	SF	scaled PGA [g]
198 (x)	Montenegro	ST64	15/04/1979	6.9	21	0.181	2.75	0.498
6335 (x)	South Iceland	ST2557	21/06/2000	6.4	15	0.127	3.92	0.498
4674 (x)	South Iceland	ST2486	17/06/2000	6.5	5	0.318	1.57	0.498
4675 (y)	South Iceland	ST2487	17/06/2000	6.5	13	0.156	3.19	0.498
55 (y)	Friuli	ST20	06/05/1976	6.5	23	0.316	1.58	0.498
128 (y)	Friuli	ST36	15/09/1976	6.0	28	0.070	7.13	0.498
6341 (x)	South Iceland	ST2497	21/06/2000	6.4	20	0.051	9.69	0.498
			mean	**6.5**	**17.9**	**0.174**	**4.26**	**0.498**

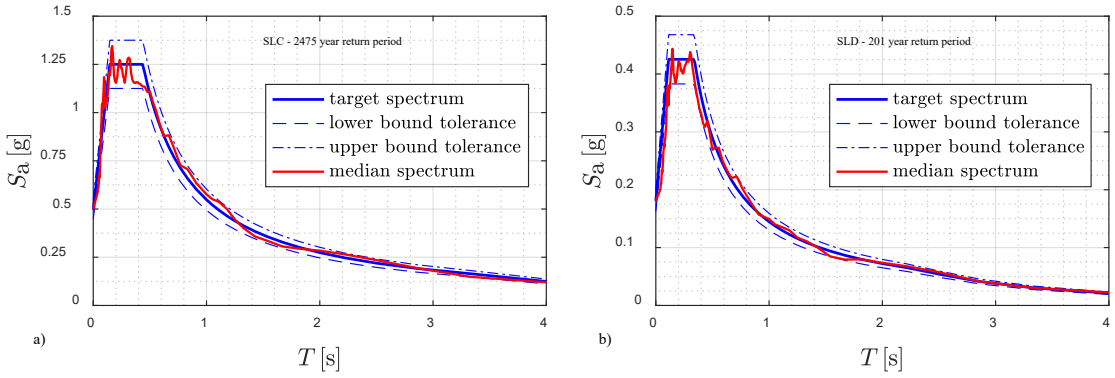

Figure 10 Comparison between target response spectrum and median response spectrum of the seven selected records for the two limit states: a) SLC; b) SLD

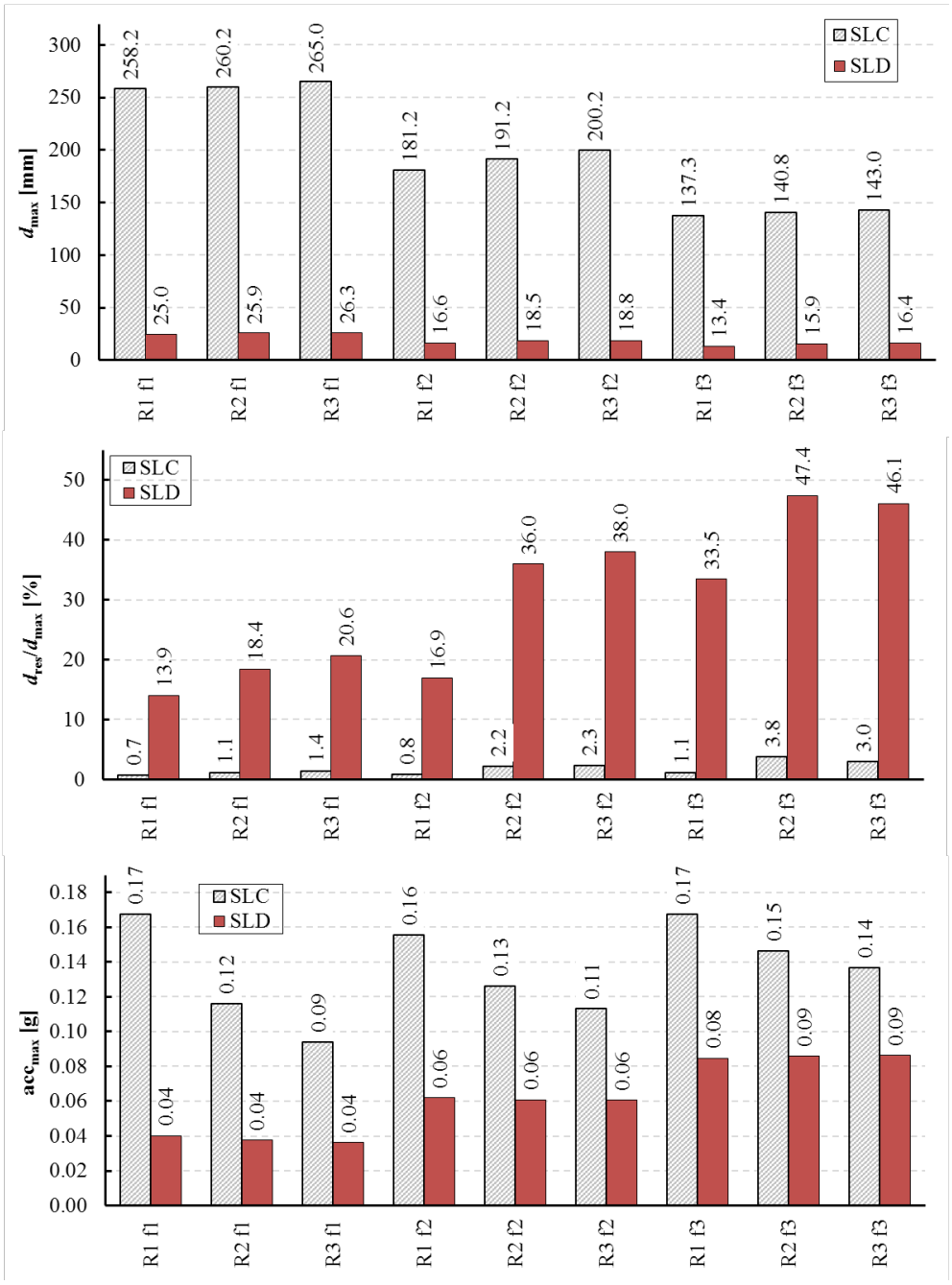

Figure 11 Seismic performance in terms of maximum displacement (top), residual displacement ratio (center) and maximum absolute acceleration (bottom) of the CSS isolation system with different parameters

Different performance requirements apply to the two considered limit states: at SLC, the collapse-prevention performance level is required, while extensive damage and plasticization of structural and non-structural elements are allowed; at SLD, the immediate-occupancy performance level for structural elements is typically required, with low-to-moderate damage of the non-structural elements. The two performance requirements are checked for the base-isolation system accordingly. For the SLC earthquake level, the isolators must be able to accommodate the displacement demand, which is the primary design parameter for the isolation system. Therefore, the maximum displacement $d_{\max}$ is an important parameter at SLC. For low-intensity frequent earthquakes corresponding to SLD level, the acceleration induced in the isolated structure must be sufficiently low to prevent damage in non-

structural elements and acceleration-sensitive equipment [51], [64]. The re-centering capability is an important function of the isolation system for both earthquake levels; therefore, the residual displacements must be checked in view of serviceability requirements and possible accrual of displacements in case of aftershocks or future events [28]. The results in terms of average maximum displacement ($d_{\max}$), average residual displacement normalized by maximum displacement ($d_{\text{res}}/d_{\max}$), and average maximum absolute acceleration ($\text{acc}_{\max}$) over the seven earthquake records for both SLC and SLD are calculated for the CSS isolation system, and the results are summarized in the histograms of Figure 11. As reasonably expected, the maximum displacement is highly dependent on the friction coefficient: the friction class f_3 exhibits an average maximum displacement that is around 40-45% lower than the friction class f_1. The radius of curvature has little influence on the maximum displacement, with a moderate increase (of around 10%) when passing from R_1 to R_3. The re-centering capability is influenced by both R_{eff} and the friction class, which is consistent with the expression of d_{rm} in Eq. (3). In particular, the worst re-centering behavior is observed in CSS isolation systems having large radius of curvature combined with high friction coefficient – as an example, the ratio $d_{\text{res}}/d_{\max}$ for the $R_3 f_3$ system is 46.1%, which means that the residual displacement is almost 50% of the maximum displacement.

5.3. Analysis of the time history response of CSS+SMAGD system

In this subsection, the time history response of the proposed isolation layout (low-friction CSS+SMAGDs) is analyzed and compared to the time history response of the conventional CSS isolation system. The intermediate radius of curvature $R_2 = 3500$ mm (associated with undamped period $T = 3.57$ s) is considered for this analysis. To assess the performance of the systems under both high-intensity and low-intensity seismic inputs, the time history response is evaluated considering the South Iceland earthquake (ID 6341, station ST2497), and the Golbasi earthquake (ID 410, station ST161), as representative records for SLC and SLD intensity levels, respectively.

In Figure 12, the acceleration history of the South Iceland earthquake is depicted, together with the response in terms of displacement history and force-displacement loops. Three different isolation systems are compared, namely the low-friction CSS system (f_1), the high-friction CSS system (f_3) and the proposed low-friction CSS+SMAGD combined system, considering the NDC NiTi alloy for the SMA wires. The cross-sectional area parameter A_{SMAGD} is assumed to be $500\ \text{mm}^2$, while the gap displacement is set to $d_{\text{gap}} = 100$ mm. It is noted that the SMAGDs, when applied to a low-friction CSS isolation system, are engaged only for displacements $d \geq d_{\text{gap}}$. The displacement demand is significantly reduced compared to the low-friction CSS system alone. In particular, the chosen area of the SMA gap damper $A_{SMAGD} = 500\ \text{mm}^2$ is large enough to achieve a displacement demand of comparable level or even lower than that of the high-friction CSS system.

As anticipated above, the damping and stiffening contribution of the SMAGD are strictly related to the size of the gap damper itself. Figure 13 shows the effect of three different areas A_{SMAGD} on the displacement mitigation and on the force-displacement loops of the combined CSS+SMAGD system. Evidently, higher values of A_{SMAGD} imply higher stiffening effects as the axial stiffness coefficients of the SMAGD k_1, k_2 are linearly proportional to the value of A_{SMAGD}, cf. Eqns. (7), and also higher damping forces F_y, F_u, related to higher supplemental energy dissipation capabilities. The design procedure, developed in this paper and previously described in Section 5, fully incorporates these two effects through an appropriate calculation of the effective stiffness k_{eff} and of equivalent viscous

damping ξ_{eff} that depend upon A_{SMAGD}. While increasing the damper size reduces the displacement more effectively, in the next subsections it will be shown that too high values of A_{SMAGD} may have the counter effect of increasing the absolute acceleration and should be avoided. Strictly speaking, for $A_{SMAGD} = 250\ \text{mm}^2$ the SMAGD would exceed its maximum displacement $d > d_u$ and, thus, would lose its superelastic behavior if a length $L_{SMAGD} = 2000\ \text{mm}$ is chosen. Therefore, the force-displacement loops shown in Figure 13 are not strictly consistent with the SMA material properties shown in Figure 9, and a larger length of the SMAGD must be adopted. More details on the design selection of L_{SMAGD} will be given in subsection 5.5.

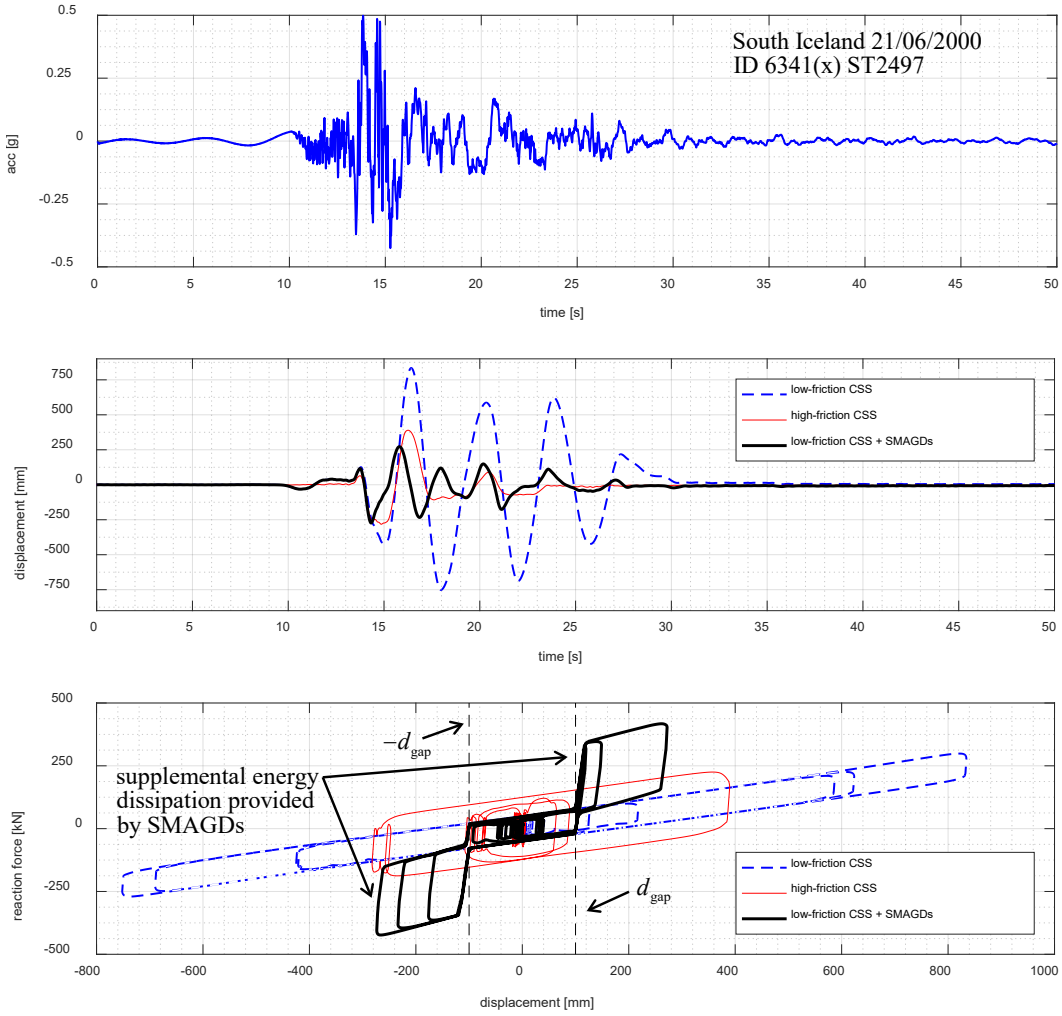

Figure 12 Response to high-intensity ground motions: acceleration time history of the South Iceland earthquake (top), displacement response of different isolation systems (middle) and force-displacement loops (bottom)

A key design parameter to optimize the displacement mitigation achieved by the SMAGD is the force ratio $FR = F_y/F_0$, i.e. the ratio between the yield strength of the SMAGD and the characteristic strength of the CSS isolators. Figure 14 illustrates the results (in terms of displacement time history and force-displacement loops) obtained with two different SMAGDs: the former using NDC NiTi alloys, the latter using GAC NiTi alloys. It is clearly seen that the two responses are comparable to each other, despite the different value of the area A_{SMAGD} being 50% higher in the GAC NiTi SMAGD compared to the NDC NiTi SMAGD. This is due to the fact that, the force ratio of the two gap damper systems is almost identical ($FR = 5.20$ and $FR = 5.25$), since this depends upon the different

materials parameters of the two considered alloys, cf. again Table 3 and Figure 9. This is an important result, as the design of the proposed system can be carried out for a pre-defined FR to meet a target displacement demand, irrespective of the specific physical properties of the alloy. Hence, the force ratio FR is a more general concept than the cross-sectional area of the SMAGD. The slightly lower displacement attained in this example by the NDC NiTi SMAGD is likely due to the additional stiffness contribution provided by the post-yield stiffness $k_2 > 0$, whereas $k_2 = 0$ in the GAC NiTi SMAGD.

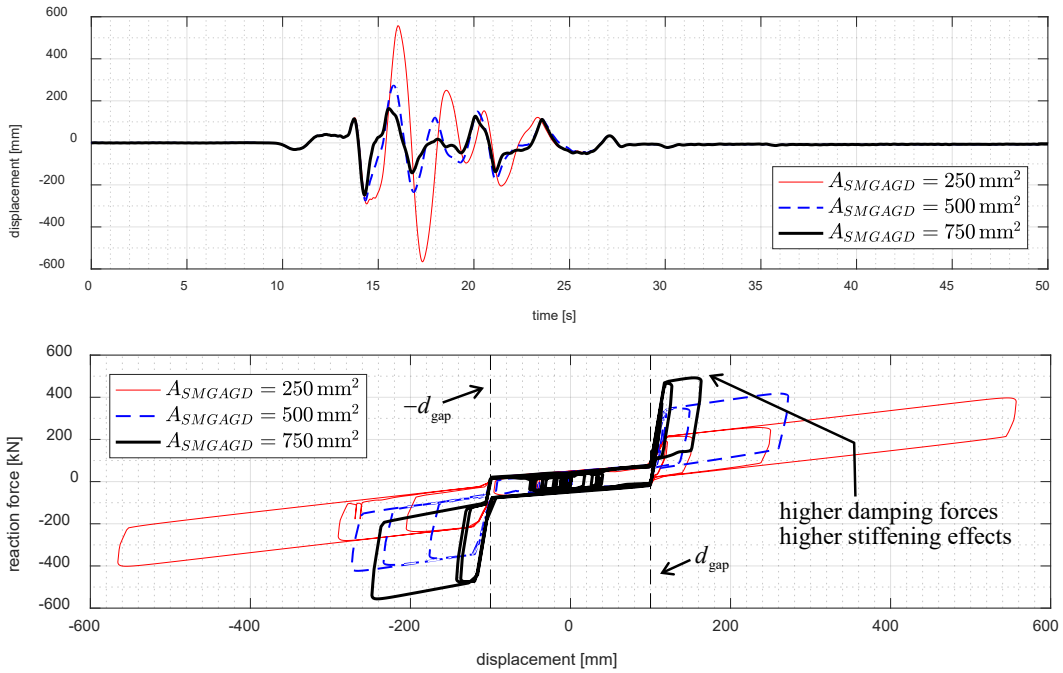

Figure 13 Response to high-intensity ground motions: effect of overall SMA wire cross-sectional area $\boldsymbol{A_{SMAGD}}$ on the displacement mitigation (top) and corresponding force-displacement loops (bottom)

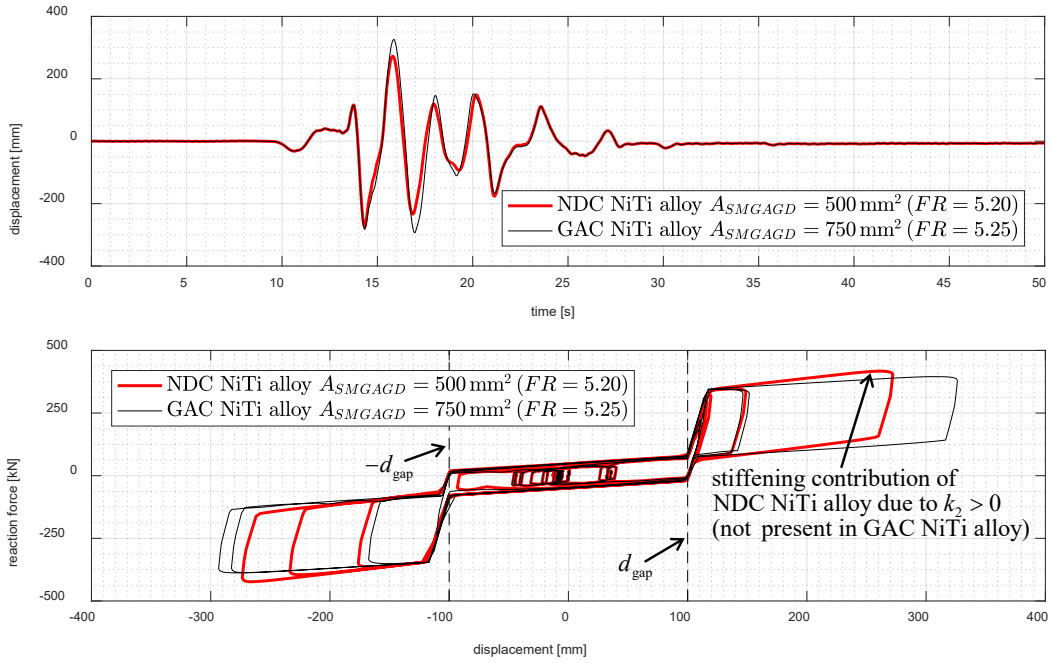

Figure 14 Response to high-intensity ground motions: combined effect of different alloys and cross-sectional areas $\boldsymbol{A_{SMAGD}}$ on the displacement mitigation (top) and corresponding force-displacement loops (bottom)

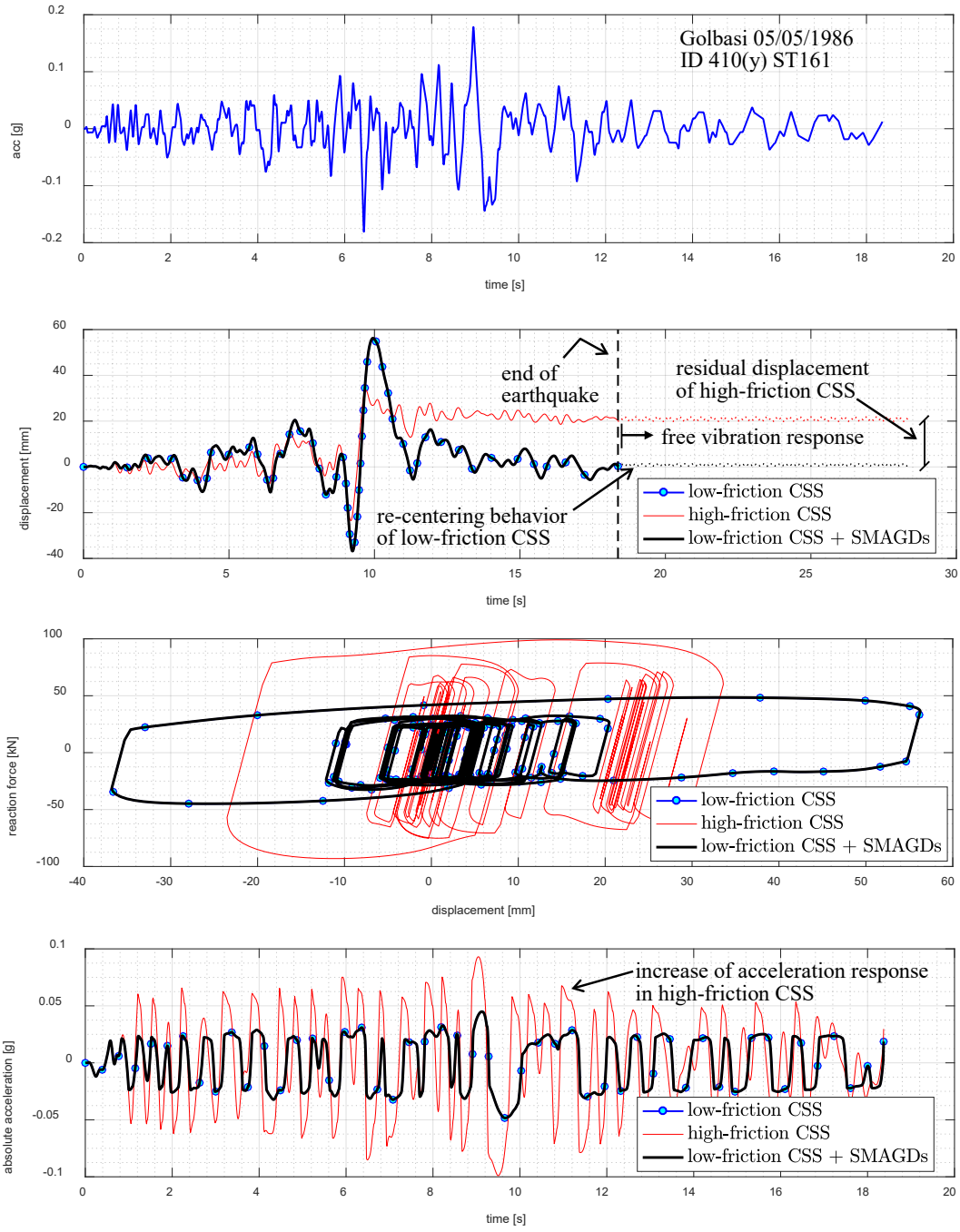

Figure 15 Response to lower-intensity ground motions: acceleration time history of the Golbasi earthquake (top), displacement response along with force-displacement loops (middle) and absolute acceleration response (bottom) of different isolation systems

With regard to low-intensity ground motions (SLD limit state), the response of the three analyzed isolation system to the Golbasi earthquake is depicted in Figure 15. The displacement history is purposely plotted over a longer time span than the actual duration of the record to examine the free vibration response and the corresponding residual displacement at the end of the earthquake event. As expected, the residual displacement generated after a low-intensity ground motion is quite large for high-friction isolation systems. In the proposed example, the residual displacement of the high-friction CSS is about 21 mm, which is more than 60% of the peak seismic displacement (32 mm). On the

contrary, the proposed low-friction CSS+SMAGD combined system benefits from the good re-centering capability related to the low friction coefficient. In particular, the gap displacement of the SMAGD has been chosen such that it is not engaged for serviceability earthquakes, which is shown in Figure 15. Consequently, the re-centering behavior and the absolute acceleration of the superstructure in the proposed low-friction CSS+SMAGDs are the same as provided by the low-friction CSS isolation system. These results highlight the beneficial effects of the phased behavior of the gap damper in eliminating undesirable effects (high accelerations and poor re-centering capability) exhibited by high friction CSSs at low-intensity excitations. In particular, the engagement of the SMAGDs can be completely prevented during frequent low-intensity ground motions by a proper assignment of the gap displacement d_{gap}. This phased behavior and the selective engagement of the gap damper facilitates the achievement of different performance criteria at various levels of the earthquake excitation. A more in-depth analysis of the seismic performance of the proposed low-friction CSS+SMAGD isolation system and a reasonable criterion for the choice of d_{gap} will be presented in the next subsections through a parametric study.

5.4. Comparison between linear analysis and NLRHAs

The design procedure developed in this paper and presented in Section 4 relies on a series of hypothesis and simplifying assumptions. Therefore, it is of utmost importance to assess the accuracy and reliability of such procedure by comparison with results obtained via more sophisticated NLRHAs. The analytical expressions presented in Section 4 can be implemented in any spreadsheet, and the developed procedure can be used either as a design tool or as a verification method. In the former case, some parameters are assigned (e.g. the target fundamental period of the isolation system, implying a certain radius of curvature and friction coefficient, the characteristics of the alloy in the SMAGD) and some others are unknown (e.g. the total area and the length of the SMA wires A_{SMAGD} and L_{SMAGD}) and must be determined to meet a target maximum displacement under the maximum credible earthquake d_{max}. In particular, the proposed procedure is able to identify the value of A_{SMAGD} (contributing to k_{eff}, ξ_{eff}) leading to a desired displacement demand of the CSS+SMAGD system from the response spectrum analysis $d_{\mathrm{max}} = S_{\mathrm{d}}\left(T_{eff}, \xi_{eff}\right)$. On the other hand, the proposed procedure can be used as a verification method, by fixing all the mechanical and geometrical parameters of the CSS+SMAGD system (which implies that both T_{eff} and ξ_{eff} are known) and calculating the expected maximum displacement d_{max} under the maximum credible earthquake.

In this subsection, the second approach is used, and the validation of the linear design procedure is carried out by computing the expected maximum displacement $d_{\mathrm{max}}^{\mathrm{lin}}$ for a pre-determined set of system parameters and comparing this value to the maximum displacement obtained via NLRHAs $d_{\mathrm{max}}^{\mathrm{NLRHA}}$. The value $d_{\mathrm{max}}^{\mathrm{NLRHA}}$ represents the average maximum displacement considering the seven spectrum-compatible accelerograms at SLC, previously presented in subsection 5.2 and whose details were given in Table 5. Therefore, results from design procedure and from NLRHAs are consistent with each other as they are based on the same design response spectrum. For the sake of generality, two gap displacements $d_{\mathrm{gap}} = 50$ mm and $d_{\mathrm{gap}} = 100$ mm, four cross-sectional areas of the SMA wires $A_{SMAGD} = 100, 250, 500, 750\ \mathrm{mm}^2$ (which are labelled as A_1, A_2, A_3, A_4), and two alloy characteristics NDC NiTi and GAC NiTi are considered. The length of the SMA wires is assumed as $L_{SMAGD} = 2000$ mm. As to the CSSs, the three radii of curvature R_1, R_2, R_3 presented in Table 1 are

investigated, while the friction class is set to f_1 (low friction coefficient), which is essential to develop an efficient isolation system with good re-centering behavior. Other combinations of moderate-friction or high-friction CSS+SMAGDs (i.e. assuming friction class f_2 or f_3 in place of f_1 in the combined system) are not examined because they fall outside the aims of the present work. The nomenclature adopted for the CSS+SMAGD isolation system is $R_i f_1 A_k$ (with $i = 1,2,3$ denoting the three curvature radii; $k = 1,2,3,4$ denoting the four SMAGD areas), which represent 12 combinations for each gap displacement and alloy, for a total number of 48 different combinations of parameters.

The histograms of average maximum displacement are plotted in Figure 16 and Figure 17 for the different parameter combinations. It can be seen that the displacement demand is larger than $d_{\text{gap}} = 100\ \text{mm}$ for all the considered parameter combinations. This means that the SMAGD is always engaged in the time history response at SLC, and it provides supplemental stiffening and energy dissipation contributions to reduce the displacement demand under the maximum credible earthquake. Indeed, by comparing the displacements obtained with the proposed CSS+SMAGD system against those exhibited by the CSS isolation system alone (shown earlier in the top part of Figure 11), a remarkable reduction of the displacement demand is observed, ranging from around 10% for $A_{SMAGD} = A_1$, up to even more than 50% for $A_{SMAGD} = A_4$. Furthermore, the results from the linear analysis are in excellent agreement with the maximum displacements obtained from NLRHAs: in particular, the actual displacement demand from NLRHAs is slightly underestimated by the linear analysis for lower values of the A_{SMAGD} parameter (especially for $A_1 = 100\ \text{mm}^2$) and is slightly overestimated for higher values of the A_{SMAGD} parameter (especially for $A_4 = 750\ \text{mm}^2$). Strictly speaking, for $d_{\text{gap}} = 50\ \text{mm}$ for some parameter combinations, especially those combinations with small SMAGD areas (e.g. $R_1 f_1 A_1$), d_{max} would exceed the maximum SMAGD displacement d_u for the chosen length L_{SMAGD}. This implies that the SMAGD would be under-designed for the considered earthquake intensity level. To guarantee a superelastic behavior , a larger length L_{SMAGD} should be selected – more details on the proper selection of the length L_{SMAGD} will be given in the next subsection.

Among all the considered cases, the highest relative error between design procedure and NLRHA is around 24% and it is obtained for the isolation system $R_1 f_1 A_1$, $d_{\text{gap}} = 100\ \text{mm}$ and SMAGD realized with GAC NiTi alloy. For other parameter combinations, the relative error is much lower, of the order of 5-15%, which is acceptable considering the simplifications introduced in the design procedure. To this aim, the value of the ratio $d_{\text{max}}^{\text{lin}}/d_{\text{max}}^{\text{NLRHA}}$ is computed for each set of 12 CSS isolation systems corresponding to an assigned SMAGD (either with NDC NiTi or with GAC NiTi alloy). The mean value and the coefficient of variation (CoV) of the ratio $d_{\text{max}}^{\text{lin}}/d_{\text{max}}^{\text{NLRHA}}$ represent measures of accuracy and of precision of the linear analysis, respectively. In particular, the mean ratio $d_{\text{max}}^{\text{lin}}/d_{\text{max}}^{\text{NLRHA}}$ is 1.00 for NDC NiTi alloy with both the gap displacements, and 0.94 and 0.95 for GAC NiTi alloy with either gap displacement; the related coefficient of variation (CoV) ranges from 9.71% to 12.11%, which indicates that the design procedure is accurate and precise.

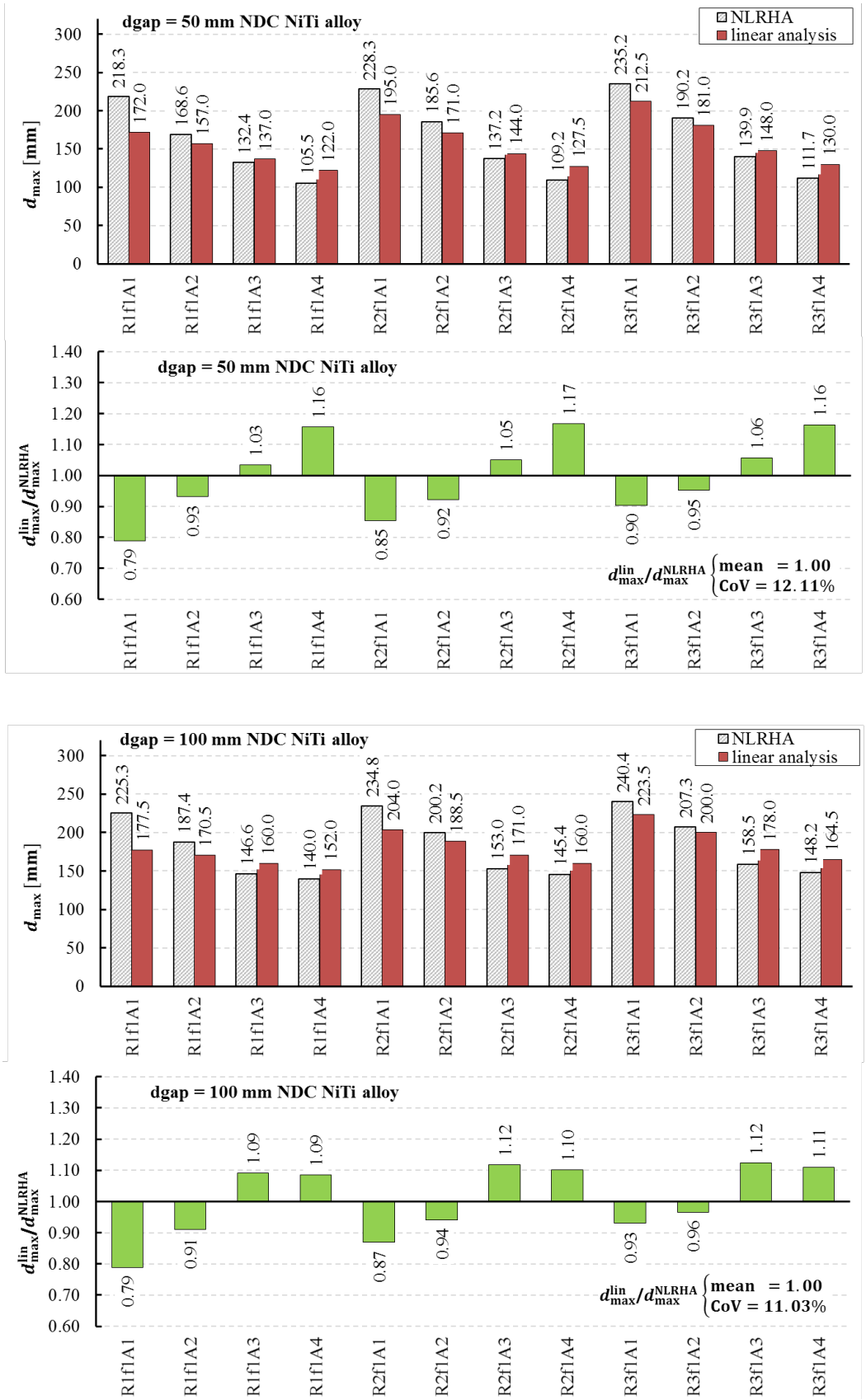

Figure 16 Maximum displacement at SLC from linear procedure d_{max}^{lin} and NLRHAs d_{max}^{NLRHA} and relevant $d_{max}^{lin}/d_{max}^{NLRHA}$ ratio for SMAGD with NDC NiTi alloy: $d_{gap} = 50$ mm (top); $d_{gap} = 100$ mm (bottom)

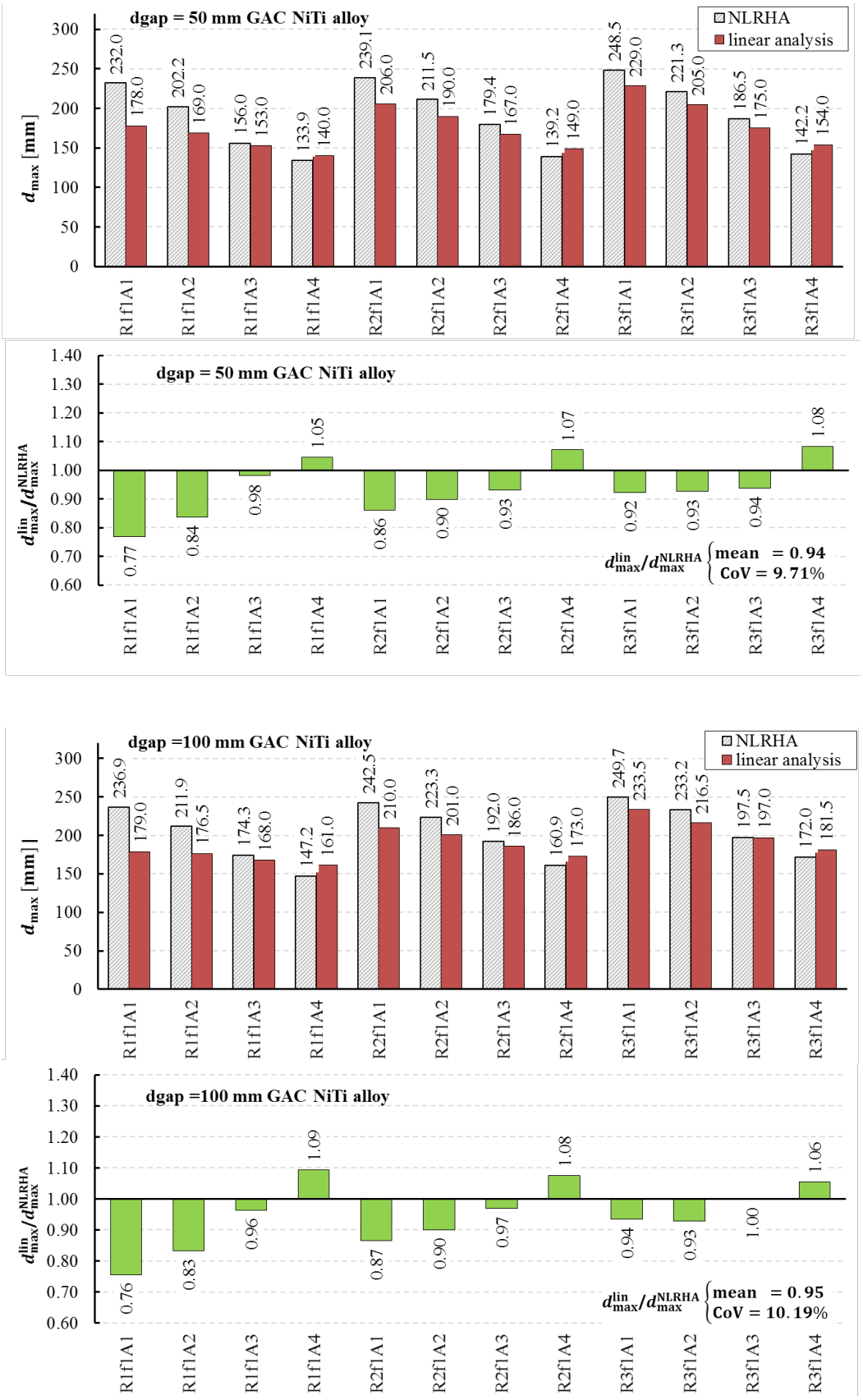

Figure 17 Maximum displacement at SLC from linear procedure $\boldsymbol{d_{max}^{lin}}$ and NLRHAs $\boldsymbol{d_{max}^{NLRHA}}$ and relevant $\boldsymbol{d_{max}^{lin}/d_{max}^{NLRHA}}$ ratio for SMAGD with GAC NiTi alloy: $\boldsymbol{d_{gap} = 50\ mm}$ (top); $\boldsymbol{d_{gap} = 100\ mm}$ (bottom)

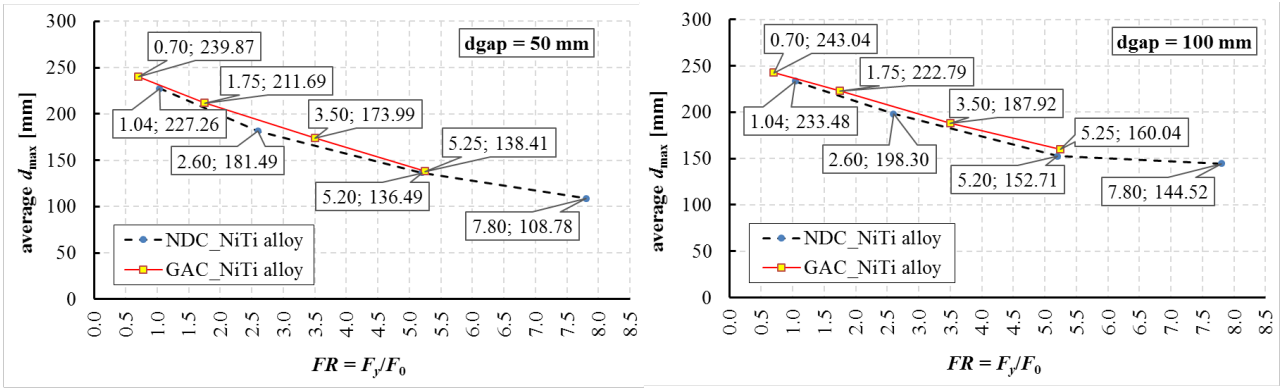

Figure 18 Effect of the force ratio $\boldsymbol{FR = F_y/F_0}$ on the average maximum displacement at SLC for $\boldsymbol{d_{gap} = 50\ mm}$ (left) and $\boldsymbol{d_{gap} = 100\ mm}$ (right)

For an equal value of A_{SMAGD}, the results obtained with the two different alloys are not comparable to each other, which has already been shown in Figure 14 when analyzing the time history response. A key design parameter is the force ratio $FR = F_y/F_0$, which quantifies the additional damping and stiffness contribution provided by the SMAGD in relationship to the characteristic strength of the CSS isolation system. Indeed, Figure 18 shows that the two alloys follow a very similar trend in terms of the FR parameter, despite the different material parameters and constitutive behavior (cf. Figure 9). In particular, the maximum displacement decreases with the increase of FR: the tags reported besides each data point (first and second figure denoting the FR ratio and the corresponding $d_{\max}$, respectively) indicate that the considered four values of A_{SMAGD} correspond to four non comparable values of FR in the two alloys (owing to the differences in the yield stress F_y). Slightly lower values of $d_{\max}$ are obtained for the NDC NiTi alloy for comparable values of FR, which is consistent with the additional stiffening effects induced by the hardening behavior (post-yield stiffness $k_2 > 0$) in the NDC NiTi alloy, which is not present in the GAC NiTi SMAGD (as $k_2 = 0$). Apart from these minor differences, the relevant $d_{\max} - FR$ plots are in reasonable agreement between the two alloys. These results suggests adopting FR (rather than A_{SMAGD}) as main parameter to quantify the SMAGD size in the parametric study of the next subsection.

5.5. Seismic performance of CSS+SMAGD system via parametric study

The seismic performance of the proposed low-friction CSS+SMAGD isolation system is analyzed through a parametric study. In a design stage, to prevent the engagement of the SMAGD for low-intensity frequent earthquakes at SLD the gap displacement of the SMAGD can be calculated through the following recommended formula

$$d_{\text{gap}} \geq \gamma_R \cdot \gamma_{IS} \cdot d_{\max}^{SLD} . \tag{16}$$

where γ_R is a reliability factor assumed as 1.1, γ_{IS} is an amplification factor of seismic displacement (or safety factor), whose recommended values are $\gamma_{IS} = 1.2$ for buildings or other civil engineering structures, and $\gamma_{IS} = 1.5$ for bridges [29], and $d_{\max}^{SLD}$ represents the displacement of the low-friction CSS isolation system at SLD. Based on Eq. (16) and considering the results shown in Figure 11, a value of $d_{\text{gap}} = 50$ mm is assumed in the design. Five different values of the force ratio $FR =$ 1,2,4,6,8 are explored, which comprise the range of values examined in the previous subsection (cf.

Figure 18), and the corresponding nomenclature of the isolation system is $R_i f_1 FR_k$ ($k = 1,2,4,6,8$). Additionally, the length L_{SMAGD} should be chosen large enough to guarantee a superelastic behavior of the SMAGD over the entire response history. This is inherently related to the maximum recoverable strain of the SMA wires ε_u. In particular, the displacements experienced by the SMAGD should not exceed the ultimate displacement d_u at which the reversible austenite to martensite phase transformation is completed. To this aim, a first estimate of L_{SMAGD} is made, then the corresponding maximum displacement during extreme earthquakes at SLC is computed and the following condition is checked

$$L_{SMAGD} \geq \left(\gamma_R \cdot \gamma_{IS} \cdot d_{\max}^{SLC} - d_{\text{gap}}\right)/\varepsilon_u \tag{17}$$

where the meaning of the coefficients γ_R and γ_{IS} has already been given above. If condition (17) is violated for the selected length L_{SMAGD} of the previous step, then a larger value should be considered and the condition (17) should be checked again.

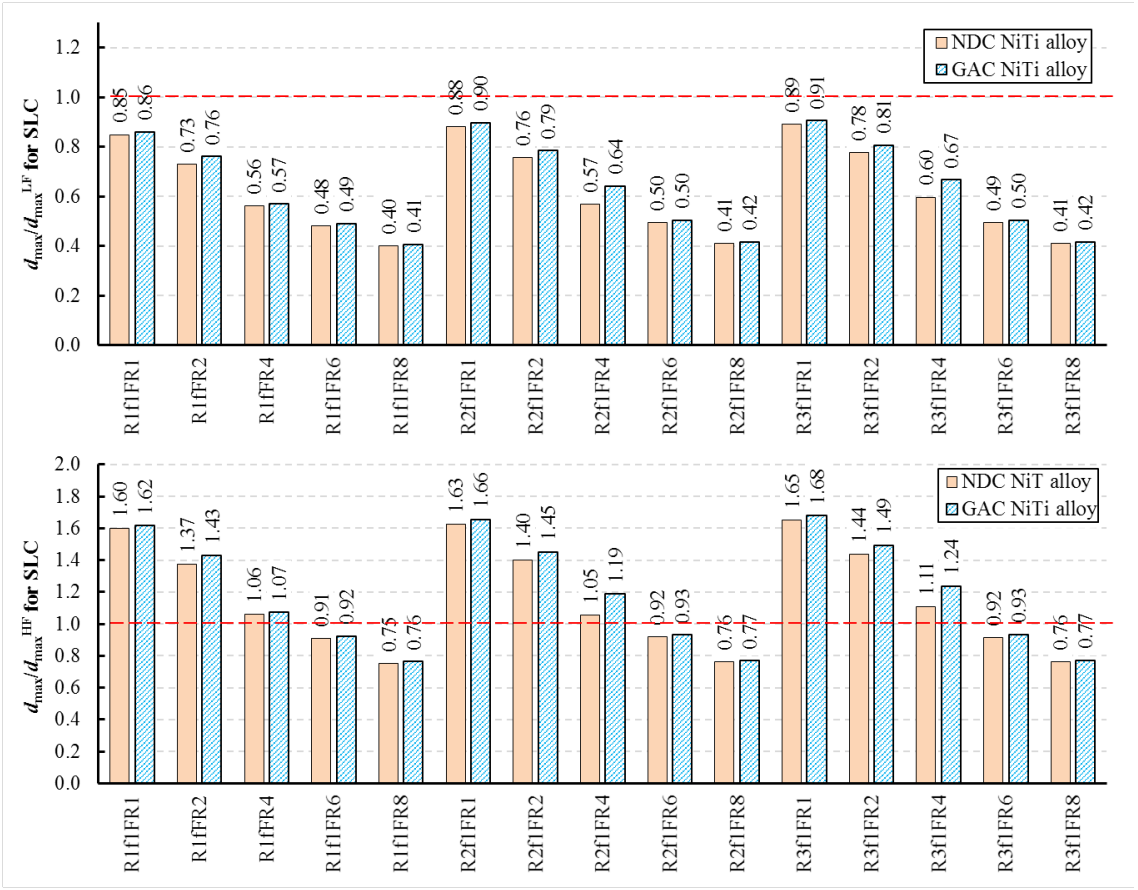

Figure 19 Seismic performance in terms of maximum displacement demand at SLC of proposed isolation system compared to low-friction CSS (top) and high-friction CSS (bottom)

In order to highlight the advantages of the proposed low-friction CSS+SMAGD isolation layout against the conventional CSS isolation system, the results are shown in a normalized format. With regard to the displacement demand, the ratios $d_{\max}/d_{\max}^{\text{LF}}$ and $d_{\max}/d_{\max}^{\text{HF}}$ are calculated at SLC earthquake level, with $d_{\max}^{\text{LF}}$ and $d_{\max}^{\text{HF}}$ denoting the average displacement demand of low-friction CSS (f_1 friction class) and high-friction CSS (f_3 friction class), respectively. With regard to the residual displacements, the ratios $d_{\text{res}}/d_{\text{res}}^{\text{LF}}$ at both SLC and SLD earthquake levels are plotted, with $d_{\text{res}}^{\text{LF}}$

denoting the average residual displacement of the low-friction CSS, which provides the best re-centering capability among the CSS isolation systems. Finally, with regard to the absolute acceleration response, the ratios $\mathrm{acc_{max}}/\mathrm{acc_{max}^{HF}}$ are plotted at both SLC and SLD earthquake levels, as well as the ratio $\mathrm{acc_{max}}/\mathrm{acc_{max}^{LF}}$ at SLD earthquake level for additional considerations in terms of serviceability requirements for low-intensity ground motions, with $\mathrm{acc_{max}^{HF}}$ and $\mathrm{acc_{max}^{LF}}$ denoting the average maximum absolute acceleration of the high-friction and low-friction CSS isolation system, respectively. The results are shown in Figure 19, Figure 20 and Figure 21 for each combination of parameters being reported along the horizontal axis.

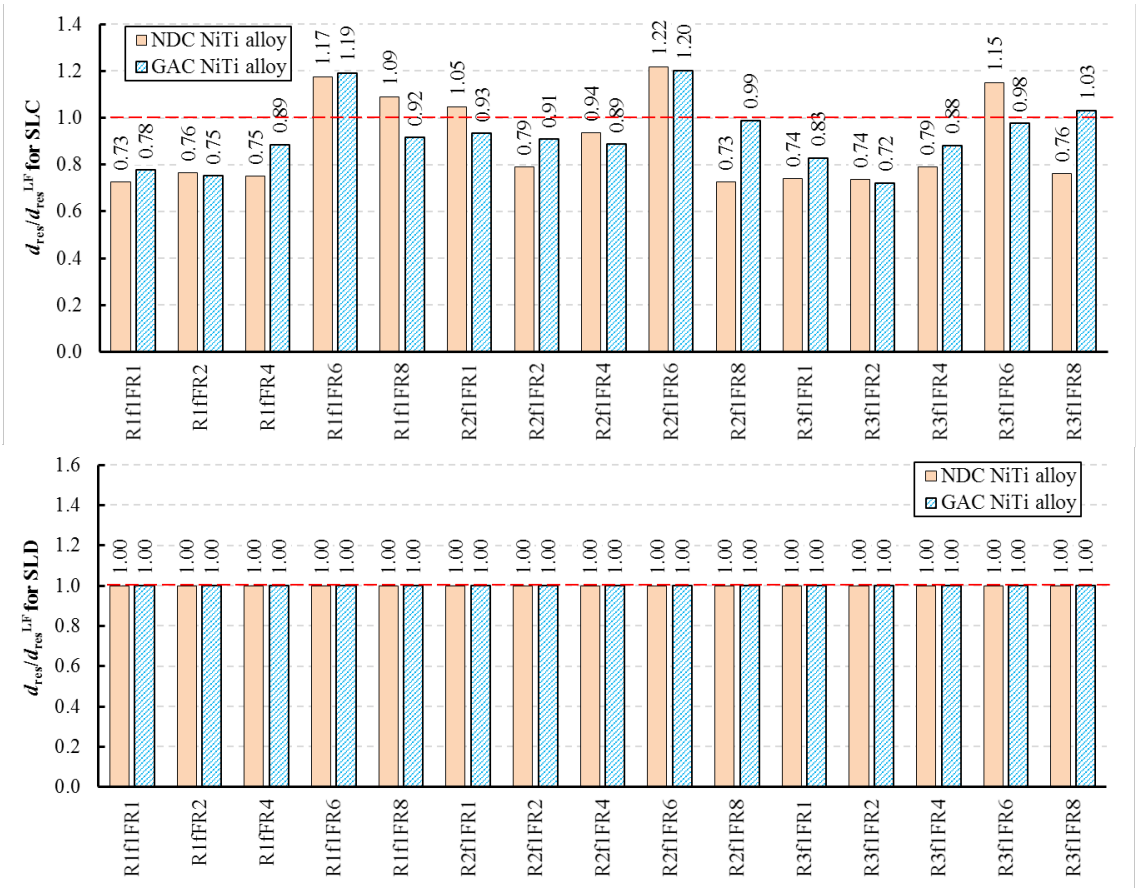

Figure 20 Seismic performance in terms of residual displacement of proposed isolation system compared to low-friction CSS at SLC (top) and SLD (bottom)

By examining the results shown in the figures, it emerges that the proposed low-friction CSS+SMAGD isolation layout outperforms the conventional CSS isolation system at both SLD and SLC earthquake levels, considering the different performance requirements. In particular, the following conclusions can be drawn:

1) The proposed system is able to reduce the displacement demand in relation to the adopted force ratio FR. For $FR \geq 4$, the resulting $d_{\max}$ is of comparable order or even lower than the displacement demand of high-friction CSS, with an achieved reduction of more than 45% (up to 60% for $FR = 8$) in comparison with the displacement demand of low-friction CSSs.
2) The SMAGD does not impair the re-centering behavior at SLC and SLD; indeed, the system is characterized by a good re-centering capability, comparable to that of the low-friction CSS. At SLC the residual displacement can be slightly lower or slightly higher than the value $d_{\mathrm{res}}^{\mathrm{LF}}$,

whereas at SLD the value $d_{\mathrm{res}}^{\mathrm{LF}}$ of the low-friction CSS is not modified at all. This occurs because the SMAGD is not engaged for low-to-moderate seismic intensity levels typical of SLD earthquakes. This result confirms that in the proposed realization scheme the phased behavior of the SMAGD provides supplemental stiffening and damping to the isolation system without impairing its re-centering capability, and thus outperforms high-friction CSS systems or combination of low-friction CSS systems with supplemental energy dissipation devices that do not have a phased behavior, e.g., fluid viscous dampers.

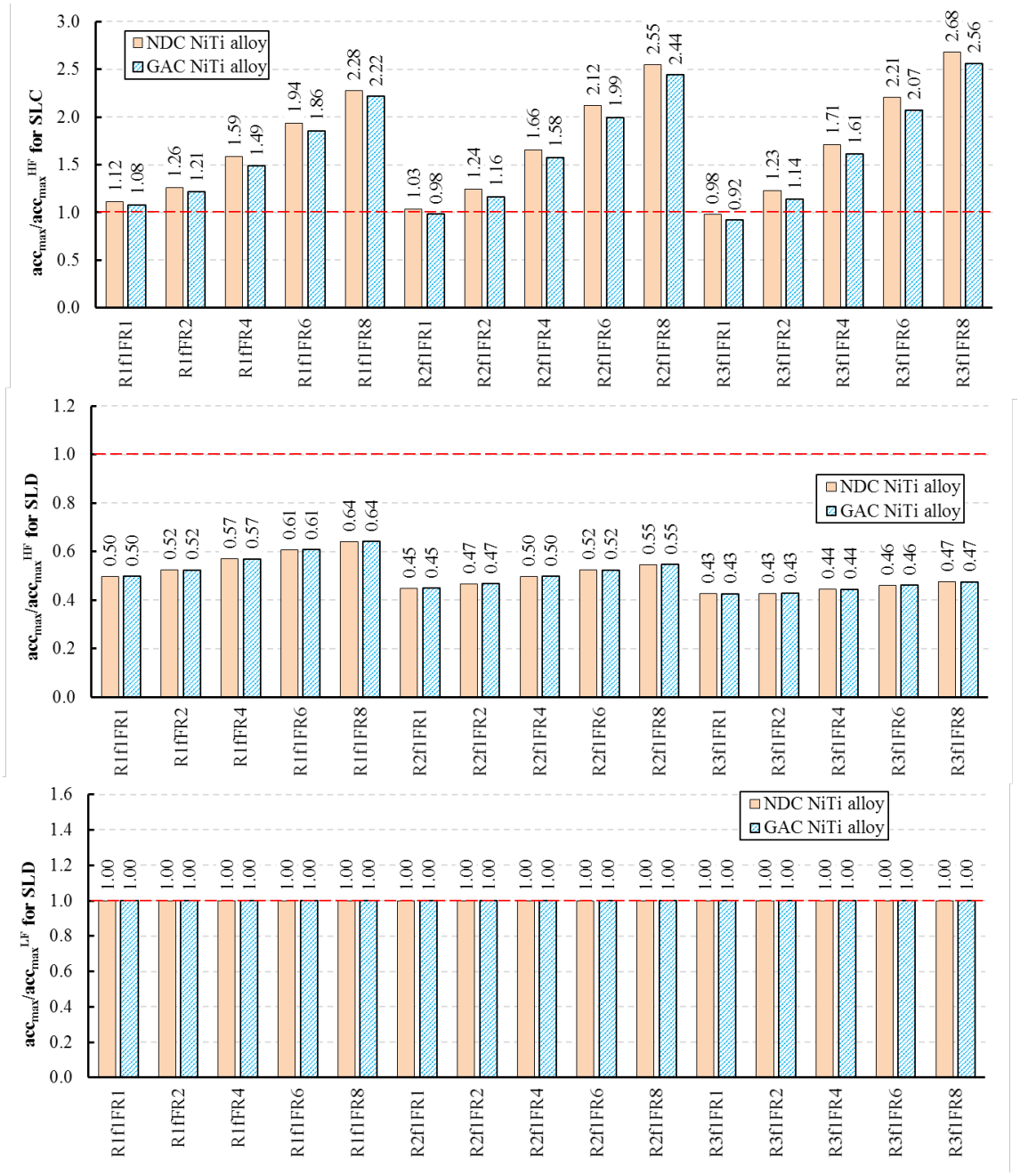

Figure 21 Seismic performance in terms of maximum absolute acceleration of proposed isolation system compared to high-friction CSS at SLC (top), SLD (middle), and compared to low-friction CSS at SLD (bottom)

3) The SMAGD produces an increase in the superstructure absolute acceleration response at SLC in relationship to the adopted force ratio FR. This counter effect is inherent to the engagement

of the gap damper, and is typical of any gap damper scheme [31]. However, some remarks should be made in this context depending on the limit state considered. In most practical cases, the acceleration response is more important for frequent earthquakes typical of SLD, where the protection of non-structural components is of major concern, whereas at SLC a collapse prevention performance level should be primarily guaranteed, which is primarily related to the displacement demand. The increase of $\mathrm{acc}_{\max}$ only occurs at SLC, whereas at SLD SMAGDs are not engaged and the acceleration response is exactly the same as that of the low-friction CSS, therefore much lower (around 40-50% lower) than the value obtained with high-friction CSSs $\mathrm{acc}_{\max}^{\mathrm{HF}}$.

4) The design choice of $d_{\mathrm{gap}} = 50\,\mathrm{mm}$, motivated by Eq. (16), is suitable for preventing the engagement of the SMAGD for low-intensity ground motions associated with the SLD earthquake level. Indeed, the results in terms of residual displacement and absolute acceleration at SLD coincide with those of the low-friction CSS isolation system. Moreover, the results obtained for the two examined NiTi alloys are comparable to each other, thus confirming that the force ratio FR is a general parameter governing the design of the proposed system, regardless of the specific material properties of the adopted SMA wires.

5.6. Comparison between hysteretic gap damper and SMAGD

An alternative isolation system based on hysteretic gap dampers has been addressed by the authors recently [50]. This scheme has been illustrated in Figure 3, and the cumulative damage effect, inherent to the hysteretic nature of the gap dampers, has already been critically discussed as a main motivation for developing the SMAGD system in Figure 5. It is, therefore, interesting to quantify the advantages of the proposed SMA-based gap dampers over the hysteretic gap dampers when the associated CSS isolation system is subjected to the same pulse-like seismic excitation. To this aim, the same case study structure analyzed in [50] is addressed, namely a one-bay one-storey steel frame isolated with four CSSs at the corners, as depicted in Figure 22. Shake-table tests were performed on this structure mounting two different classes of CSSs, namely low-friction and high-friction CSSs. Details of the testing equipment and of the frictional characteristics of the isolators can be found in previous works [28], [50]. In line with the previous paper [50], the seismic excitation analyzed consists in a sequence of three repetitions of the Campano Lucano 1980 earthquake. A finite element model of the steel frame isolated with four CSS bearings (without any gap damper) has been preliminarily set up in OpenSees [50] to calibrate the velocity-dependent friction model of the sliding pendulum bearings. As shown in Figure 22, a good agreement between OpenSees numerical model and experimental shake-table test results in terms of top floor displacement response is achieved for both the low-friction and the high-friction cases. A notably different response is observed in the two cases: as expected, the low-friction CSSs suffer from higher displacements than the high-friction CSSs. Nevertheless, the poor re-centering behavior of high-friction CSSs combined with the pulse-like nature of the selected earthquake (with a pronounced directivity effect) produces a significant accrual of residual displacements in the three repetitions that, in turn, generates an increase of the peak displacement.

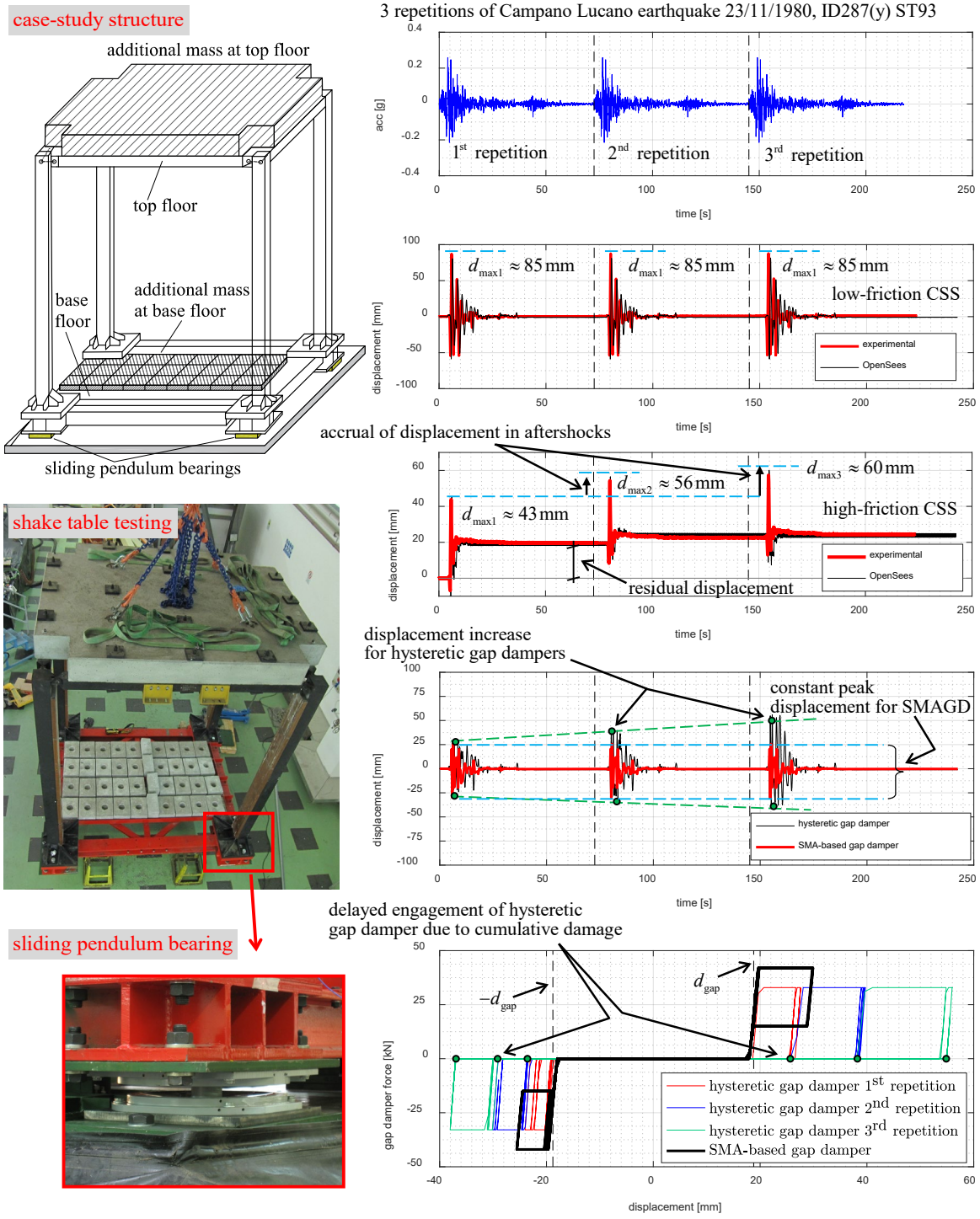

Figure 22 Case study structure for comparison between hysteretic gap damper [50] and SMA-based gap damper (left) and relevant time-history response (right) for different isolation systems

Having properly calibrated the velocity-dependent friction model of the CSSs, the same seismic input is then applied numerically to the OpenSees model implementing low-friction CSSs combined with either the hysteretic gap dampers (previous solution) or the SMAGDs (proposed solution). The hysteretic gap dampers are designed according to the energy-based design procedure described in [50], while the SMAGDs are designed according to the iterative displacement spectral analysis procedure described in Section 4 of this paper. For consistency reasons, both the procedures assume

a target maximum displacement for the selected earthquake of 25 mm. The obtained displacement time-history responses along with the related hysteretic behavior of the two gap damper systems are plotted in the right-bottom part of Figure 22. Based on these results, it is evident that the two gap damper systems behave similarly only for the first repetition of the ground motion, wherein the effects of the cumulative damage do not manifest themselves. For the first repetition, the peak displacement attained is very close to the target displacement, thus further confirming the validity of the two adopted design procedures for the case. However, during the second and third repetition the peak displacement of the system with hysteretic gap damper increases progressively. This is due to the delayed engagement of the hysteretic gap damper, as the gap displacement gets higher and higher owing to the accumulated plastic deformation in previous cycles. On the contrary, the peak displacement of the system with SMAGD keeps constant in all the three repetitions, due to the flag-shaped behavior of the SMAs and the elimination of residual displacements upon unloading. As a result, the SMAGDs eliminate the drawbacks of cumulative damage effects exhibited by hysteretic gap dampers.

6. CONCLUSIONS

An effective base-isolation system that combines low-friction CSS with shape memory alloy gap dampers (SMAGDs) has been presented. The SMAGDs provide supplemental stiffening and energy dissipation only when the isolation system exceeds a threshold or gap displacement d_{gap} while not being engaged for displacements smaller than d_{gap}. A conceptual model of the system has been presented, based on a sliding pin and a slotted ring in order to accomplish the "gap damper" feature.

The main findings of this research work can be summarized as follows:

1) The phased behavior of the SMAGD realization scheme recommended in this paper does not impair the re-centering capability of the isolation system, since it is composed by two "tension-only" SMA-based dampers that do not provide any reaction force during the coda stage of the ground motion or during free vibration of the isolation system in the neighborhood of its undeformed configuration (cf. Figure 5).
2) The proposed SMAGDs exploit the superelastic properties and the flag-shaped hysteretic behavior of SMAs, which can eliminate drawbacks related to the cumulative damage encountered in other types of gap dampers, such as hysteretic gap dampers (cf. Figure 3).
3) The SMAGD system can be designed to keep peak displacements of the isolation system to within a desired threshold. A performance-oriented linear procedure aimed at achieving a target displacement demand of the combined CSS+SMAGD system under the maximum credible design earthquake has been developed. As an example, the target displacement demand can be chosen to be at the same level as (or even lower than) the one provided by a traditional high-friction CSS isolation system.
4) The proposed linear procedure is based on iterative displacement spectral analysis and on some simplified (yet reasonable) assumptions for the formulation of the linear equivalent mechanical properties of the SMAGD, whereas for the CSS it follows established practice. This linear procedure has been numerically validated against results from NLRHAs for a variety of system parameters, showing excellent accuracy and precision.
5) A leading design parameter of the proposed SMAGD is the force ratio $FR = F_y/F_0$ between the yield stress of the SMA-based damper and the characteristic strength of the CSS isolation

system. This parameter quantifies the additional stiffness and damping contributions provided by the SMAGD, and it is independent of the specific material parameters and constitutive models of the employed SMAs.

6) Although limited to simple unidirectional earthquake excitations (which is consistent with the nature of the present feasibility study), the seismic performance of the proposed CSS+SMAGD isolation system has been assessed through a wide parametric study including two intensities of the earthquake excitation (associated with two distinct performance requirements, namely no collapse requirements and serviceability requirements) and different CSS and SMAGD properties. The results of the parametric study have demonstrated that the phased behavior of SMAGDs avoids undesirable effects (e.g. high structural accelerations and poor re-centering capability) exhibited by alternative systems during low-intensity serviceability-level earthquakes (such as systems based on high-friction CSSs or combinations of CSS with traditional supplemental energy dissipation devices). Moreover, the system is effective to reduce the displacement demand of low-friction CSS isolation systems during extreme earthquakes, and this displacement reduction depends on the chosen FR ratio. Higher FR ratios lead to lower displacements but also produce higher superstructure absolute accelerations during extreme earthquakes as a counter effect. Therefore, the design value of FR must be properly selected in order to balance displacement reduction and acceleration increase. In conclusion, the proposed CSS+SMAGD system efficiently combines the inherent advantages of low-friction and high-friction CSS systems in a single layout.

REFERENCES

[1] Martelli A, Clemente P, De Stefano A, Forni M, Salvatori A, Recent development and application of seismic isolation and energy dissipation and conditions for their correct use, in Perspectives on European Earthquake Engineering and Seismology, (Ed: A. Ansal) Vol. 1, Springer, New York, USA 2014, 449.

[2] Caliò I, Marletta M, Vinciprova F. Seismic response of multi-storey buildings base-isolated by friction devices with restoring properties. Comput Struct 2003;81:2589–99.

[3] Castaldo P, Palazzo B, Della Vecchia P. Seismic reliability of base-isolated structures with friction pendulum bearings. Eng Struct 2015;95:80–93.

[4] Nagarajaiah, S., & Xiaohong, S. Response of base-isolated USC hospital building in Northridge earthquake. J Struct Eng ASCE 2000; 126(10), 1177-1186.

[5] Naeim F, Kelly JM. Design of Seismic Isolated Structures: From Theory to Practice. John Wiley & Sons. New York, 1999.

[6] Zayas V, Low S, Mahin S, The FPS earthquake resisting system. Report No. CB/EERC-87/01, Earthquake Engineering Research Center, University of California, Berkeley, 1987.

[7] Maurer SE webpage: https://www.maurer.eu/.

[8] FIP Industriale web page: https://www._pindustriale.it/.

[9] Mageba webpage: https://www.mageba.ch/en/.

[10] Anagnostopoulos SA, Spiliopoulos KV. An investigation of earthquake induced pounding between adjacent buildings. Earthq Eng Struct Dyn 1992; 21:289-302.

[11] Kelly JM. The role of damping in seismic isolation. Earthq Eng Struct Dyn. 1999; 28:3-20.

[12] Clark PW, Aiken ID, Kelly JM. Experimental studies of the ultimate behavior of seismically-isolated structures. Earthquake Engineering Research Center, University of California, 1997.

[13] Panchal VR, Jangid RS. Seismic response of structures with variable friction pendulum system. J Earthq Eng 2009; 13(2):193–216.

[14] Lu LY, Lee TY, Yeh SW. Theory and experimental study for sliding isolators with variable curvature. Earthq Eng Struct Dyn 2009; 40(14):1609–1627.

[15] Peng Y, Ding L, Chen J, Villaverde R. Experimental study of sliding hydromagnetic isolators for seismic protection. Journal of Structural Engineering ASCE 2019; 145(5): 04019021.

[16] Peng Y, Ding L, Chen J. Performance evaluation of base-isolated structures with sliding hydromagnetic bearings. Structural Control and Health Monitoring 2019; 26(1): e2278.
[17] Peng Y, Huang T. Sliding implant-magnetic bearing for adaptive seismic mitigation of base-isolated structures. Structural Control and Health Monitoring 2019; 26(10): e2431.
[18] Yang JN, Danielians A, Liu SC. Aseismic hybrid control systems for building structures. J Eng Mech 1991; 117: 836-853.
[19] Taniguchi T, Der Kiureghian A, Melkumyan M. Effect of tuned mass damper on displacement demand of base-isolated structures. Eng Struct 2008; 30:3478-3488.
[20] De Domenico D, Ricciardi G. Earthquake-resilient design of base isolated buildings with TMD at basement: Application to a case study. Soil Dyn Earth Eng 2018; 113: 503-521.
[21] De Domenico D, Ricciardi G. An enhanced base isolation system equipped with optimal Tuned Mass Damper Inerter (TMDI). Earthq Eng Struct Dyn 2018; 47: 1169-1192.
[22] De Domenico D, Impollonia N, Ricciardi G. Soil-dependent optimum design of a new passive vibration control system combining seismic base isolation with tuned inerter damper. Soil Dyn Earth Eng 2018; 105: 37-53.
[23] Hashimoto T, Fujita K, Tsuji M, Takewaki I. Innovative base-isolated building with large mass-ratio TMD at basement for greater earthquake resilience. Future Cities and Environment 2015; 1:9: 1-19.
[24] Medeot R. Re-centring capability evaluation of seismic isolation systems based on energy concepts. In Proceedings of the 13th world conference on earthquake engineering 2004; Vancouver, Canada, Vol. 3106.
[25] Katsaras CP, Panagiotakos TB, Kolias B. Restoring capability of bilinear hysteretic seismic isolation systems. Earthq Eng Struct Dyn 2008; 37(4): 557-575.
[26] Cardone D, Gesualdi G, Brancato P. Restoring capability of friction pendulum seismic isolation systems. Bull Earthq Eng 2015; 13(8): 2449-2480.
[27] Ponzo FC, Di Cesare A, Leccese G, Nigro D. Shake table testing on restoring capability of double concave friction pendulum seismic isolation systems. Earthq Eng Struct Dyn 2017; 46(14): 2337-2353.
[28] Quaglini V, Gandelli E, Dubini P. Experimental investigation of the re-centring capability of curved surface sliders. Struct Contr Health Monit 2017; 24(2): e1870.
[29] Quaglini V, Gandelli E, Dubini P, Limongelli MP. Total displacement of curved surface sliders under nonseismic and seismic actions: A parametric study. Struct Contr Health Monit 2017; 24(12): e2031.
[30] Gandelli E, Quaglini V. Effect of the static coefficient of friction of curved surface sliders on the response of an isolated building. J Earth Eng 2018; DOI: 10.1080/13632469.2018.1467353.
[31] Zargar H, Ryan KL, Marshall JD. Feasibility study of a gap damper to control seismic isolator displacements in extreme earthquakes. Struct Contr Health Monit 2013; 20(8): 1159-1175.
[32] Rawlinson TA, Marshall JD, Ryan KL, Zargar H. Development and experimental evaluation of a passive gap damper device to prevent pounding in base-isolated structures. Earthq Eng Struct Dyn 2015; 44(11): 1661-1675.
[33] Zargar H, Ryan KL, Rawlinson TA, Marshall JD. Evaluation of a passive gap damper to control displacements in a shaking test of a seismically isolated three-story frame. Earthq Eng Struct Dyn 2017; 46(1): 51-71.
[34] Auricchio F, Sacco E. A one-dimensional model for superelastic shape-memory alloys with different elastic properties between austenite and martensite. Int J Non-Lin Mech 1997; 32: 1101-1114.
[35] DesRoches R, McCormick J, Delemont M. Cyclic properties of superelastic shape memory alloy wires and bars. J Struct Eng ASCE 2004; 130(1): 38-46.
[36] Song G, Ma N, Li HN. Applications of shape memory alloys in civil structures. Eng Struct 2006; 28(9): 1266-1274.
[37] DesRoches R, Smith B. Shape memory alloys in seismic resistant design and retrofit: a critical review of their potential and limitations. J Earth Eng 2003; 7: 1-15.
[38] Ozbulut OE, Hurlebaus S, Desroches R. Seismic response control using shape memory alloys: a review. Journal of Intelligent Material Systems and Structures 2011; 22(14): 1531-1549.
[39] Fugazza D. Shape-memory alloy devices in earthquake engineering: mechanical properties, constitutive modelling and numerical simulations. Master's thesis, European School for Advanced Studies in Reduction of Seismic Risk (ROSE School), Pavia, Italy, 2003.
[40] Attanasi G, Auricchio F, Fenves GL. Feasibility assessment of an innovative isolation bearing system with shape memory alloys. J Earthq Eng 2009; 13: 18-39.

[41] Quaglini V, Dubini P, Poggi C. Experimental assessment of sliding materials for seismic isolation systems. Bull Earthq Eng 2012; 10: 717–740.
[42] Dolce M, Cardone D, Croatto F. Frictional behaviour of steel-PTFE interfaces for seismic isolation. Bull Earthq Eng 2005; 3(1): 75-99
[43] Lomiento G, Bonessio N, Benzoni G. Friction model for sliding bearings under seismic excitation. J. Earthq. Eng. 2013; 17: 1162–1191.
[44] Quaglini V, Bocciarelli M, Gandelli E, Dubini P. Numerical assessment of frictional heating in sliding bearings for seismic isolation. J Earthq Eng 2014; 18(8): 1198-1216.
[45] Kumar M, Whittaker AS, Constantinou MC. Characterizing friction in sliding isolation bearings. Earthq Eng Struct Dyn 2015; 44(9): 1409-1425.
[46] De Domenico D, Ricciardi G, Benzoni G. Analytical and finite element investigation on the thermo-mechanical coupled response of friction isolators under bidirectional excitation. Soil Dyn Earthq Eng 2018; 106:131-147.
[47] Furinghetti M, Pavese A, Quaglini V, Dubini P. Experimental investigation of the cyclic response of double curved surface sliders subjected to radial and bidirectional sliding motions. Soil Dyn Earthq Eng 2019; 117: 190-202.
[48] Gandelli E, Penati M, Quaglini V, Lomiento G, Miglio E, Benzoni GM. A novel OpenSees element for single curved surface sliding isolators. Soil Dyn Earthq Eng 2019; 119: 433-453.
[49] Constantinou M, Mokha A, Reinhorn AR. Teflon bearings in base isolation II: modeling. J Struct Eng 1990;116(2):455–74.
[50] De Domenico D, Gandelli E, Quaglini V. Effective base isolation combining low-friction curved surface sliders and hysteretic gap dampers. Soil Dyn Earth Eng 2020; 130: 105989.
[51] Gandelli E, Quaglini V, Dubini P, Limongelli MP, Capolongo S. Seismic isolation retrofit of hospital buildings with focus on non-structural components, Ingegneria Sismica - International Journal of Earthquake Engineering 2018; Vol. 2018 (4).
[52] De Domenico D, Falsone G, Ricciardi G. Improved response-spectrum analysis of base-isolated buildings: a substructure-based response spectrum method. Eng Struct 2018; 162: 198-212.
[53] Priestley MJN, Calvi GM, Kowalsky MJ. Displacement-based seismic design of structures. IUSS Press, Pavia 2007.
[54] Mazza F, Vulcano A. Displacement-based design procedure of damped braces for the seismic retrofitting of r.c. framed buildings. Bulletin of Earthquake Engineering 2015; 13(7): 2121-2143.
[55] Dwairi HM, Kowalsky MJ, Nau JM. Equivalent damping in support of direct displacement-based design. J Earthq Eng 2007; 11(4): 512-530.
[56] Jacobsen LS. Steady forced vibrations as influenced by damping," ASME Transactione 1930; 52(1): 169-181.
[57] McKenna F, Fenves GL, Scott MH, Jeremic B. Open System for Earthquake Engineering Simulation (OpenSees), Pacific Earthquake Engineering Research Center (PEER), Berkeley, USA 2000.
[58] OpenSeesWiki, online manual, available at: http://opensees.berkeley.edu/wiki/index.php/Main_Page.
[59] Christopoulos C, Tremblay R, Kim HJ, Lacerte M. Self-Centering Energy Dissipative Bracing System for the Seismic Resistance of Structures: Development and Validation. J Struct Eng ASCE 2008; 134(1): 96-107.
[60] Tremblay R, Lacerte M, Christopoulos C. Seismic Response of Multistory Buildings with Self-Centering Energy Dissipative Steel Braces. J Struct Eng ASCE 2008; 134(1): 108-120.
[61] NTC2018. CSLLPP - Consiglio Superiore dei Lavori Pubblici. Norme Tecniche per le Costruzioni. Gazzetta Ufficiale 495 della Repubblica Italiana, No. 42 of 20 February 2018. Rome, Italy, (in Italian).
[62] Iervolino I, Galasso C, Cosenza E. REXEL: computer aided record selection for code-based seismic structural analysis. Bull Earthq Eng 2010; 8: 339-362.
[63] Ambraseys N, Smit P, Sigbjornsson R, Suhadolc P Margaris B. Internet-Site for European Strong-Motion Data, European Commission, Research-Directorate General, Environment and Climate Programme 2002.
[64] Gandelli E, Taras A, Distl J, Quaglini V. Seismic retrofit of hospitals by means of hysteretic braces: influence on acceleration-sensitive non-structural components. Frontiers in Built Environment – Earthquake Engineering 2019; doi: 10.3389/fbuil.2019.00100.